








Article

A Holistic High-Resolution Remote Sensing Approach for Mapping Coastal Geomorphology and Marine Habitats

Evagoras Evagorou ^{1,2} , Thomas Hasiotis ^{3,*}, Ivan Theophilos Petsimeris ³, Isavela N. Monioudi ³ , Olympos P. Andreadis ³, Antonis Chatzipavlis ³ , Demetris Christofi ^{1,2} , Josephine Kountouri ^{1,2}, Neophytos Stylianou ² , Christodoulos Mettas ^{1,2} , Adonis Velegrakis ³  and Diofantos Hadjimitsis ^{1,2}

- ¹ Department of Civil Engineering and Geomatics, Faculty of Engineering and Technology, Cyprus University of Technology, Lemesos 3036, Cyprus; evagoras.evagorou@eratosthenes.org.cy (E.E.); demetris.christofi@eratosthenes.org.cy (D.C.); josefina.kountouri@eratosthenes.org.cy (J.K.); christodoulos.mettas@eratosthenes.org.cy (C.M.); d.hadjimitsis@eratosthenes.org.cy (D.H.)
 - ² ERATOSTHENES Centre of Excellence, 3012, Limassol 3036, Cyprus; neophytos.stylianou@eratosthenes.org.cy
 - ³ Department of Marine Sciences, University of the Aegean, Lesvos Isl., 81100 Mitilini, Greece; marm21023@marine.aegean.gr (I.T.P.); imonioudi@marine.aegean.gr (I.N.M.); olympos@marine.aegean.gr (O.P.A.); a.chatzipavlis@marine.aegean.gr (A.C.); afv@aegean.gr (A.V.)
- * Correspondence: hasiotis@aegean.gr

Abstract: Coastal areas have been the target of interdisciplinary research aiming to support studies related to their socio-economic and ecological value and their role in protecting backshore ecosystems and assets from coastal erosion and flooding. Some of these studies focus on either onshore or inshore areas using sensors and collecting valuable information that remains unknown and untapped by other researchers. This research demonstrates how satellite, aerial, terrestrial and marine remote sensing techniques can be integrated and inter-validated to produce accurate information, bridging methodologies with different scope. High-resolution data from Unmanned Aerial Vehicle (UAV) data and multispectral satellite imagery, capturing the onshore environment, were utilized to extract underwater information in Coral Bay (Cyprus). These data were systematically integrated with hydroacoustic including bathymetric and side scan sonar measurements as well as ground-truthing methods such as drop camera surveys and sample collection. Onshore, digital elevation models derived from UAV observations revealed significant elevation and shore-line changes over a one-year period, demonstrating clear evidence of beach modifications and highlighting coastal zone dynamics. Temporal comparisons and cross-section analyses displayed elevation variations reaching up to 0.60 m. Terrestrial laser scanning along a restricted sea cliff at the edge of the beach captured fine-scale geomorphological changes that arise considerations for the stability of residential properties at the top of the cliff. Bathymetric estimations derived from PlanetScope and Sentinel 2 imagery returned accuracies ranging from 0.92 to 1.52 m, whilst UAV reached 1.02 m. Habitat classification revealed diverse substrates, providing detailed geoinformation on the existing sediment type distribution. UAV data achieved 89% accuracy in habitat mapping, outperforming the 83% accuracy of satellite imagery and underscoring the value of high-resolution remote sensing for fine-scale assessments. This study emphasizes the necessity of extracting and integrating information from all available sensors for a complete geomorphological and marine habitat mapping that would support sustainable coastal management strategies.

Keywords: satellite imagery; aerial mapping; terrestrial laser scanning; hydroacoustics; topography; coastal bathymetry; habitat mapping; beach erosion; Cyprus



Academic Editors: Günther Retscher, Javier Marcello, Paolo Dabove and Gino Dardanelli

Received: 27 February 2025

Revised: 10 April 2025

Accepted: 14 April 2025

Published: 17 April 2025

Citation: Evagorou, E.; Hasiotis, T.; Petsimeris, I.T.; Monioudi, I.N.; Andreadis, O.P.; Chatzipavlis, A.; Christofi, D.; Kountouri, J.; Stylianou, N.; Mettas, C.; et al. A Holistic High-Resolution Remote Sensing Approach for Mapping Coastal Geomorphology and Marine Habitats. *Remote Sens.* **2025**, *17*, 1437. <https://doi.org/10.3390/rs17081437>

Copyright: © 2025 by the authors. Licensee MDPI, Basel, Switzerland. This article is an open access article distributed under the terms and conditions of the Creative Commons Attribution (CC BY) license (<https://creativecommons.org/licenses/by/4.0/>).

1. Introduction

Coastal zones are multifunctional environments that concentrate socio-economic conflicting interests, pressures and impacts [1]. They constitute diverse and dynamic ecosystems hosting habitats and bio-communities, often of very high ecological value [2], which are threatened by both human activities and natural processes [3–6]. These considerations are more emphatic for the low-lying sedimentary coastlines (sandy coastlines—beaches), especially those consisting of touristic beaches. These are valuable habitats [2], often having high hedonic value [7] as they are the focus of the currently dominant sand, sun and sea (3S) tourism [8]. Beaches form secure and protective backshore ecosystems, and growing human infrastructures/assets can potentially cause coastal erosion and flooding [9–11]. The projected increases in mean and extreme sea levels under climate change are of particular importance, as the impact can alter the geomorphology of beaches and their various ecosystem services [3,10–12].

Beaches form coastal sediment ‘stores’ that are controlled by sea level changes, local morphology and hydrodynamics and the available sediment supply [13]. Beach sediments, mobilized by nearshore hydrodynamics, move between the landward natural (e.g., cliffs, vegetated dunes) and/or artificial (backshore infrastructure/assets) boundary of the active dry beach and the closure depth, the point of the subtidal beach profile, where surface wave action no longer impacts the seabed sediments [14]. Thus, beach sediments transported beyond the closure depth by extreme storm events cannot return to the beach store, being ‘lost’ to deeper waters. It appears that for the beach to remain stable, these losses must be balanced by new sediments, such as locally produced biogenic sediments, fluvial inputs, and sedimentary material from neighboring beaches and/or the erosion of coastal cliffs [15–18]. The implication is that beaches characterized by small dimensions, low biogenic productivity, diminishing fluvial inputs and isolation from lateral coastal sediment supply are vulnerable to erosion. This becomes even more urgent in low-lying touristic coastal areas, and especially those of islands, where the majority of the beaches are small and laterally constrained by coastal cliff promontories (pocket beaches), since sea-level rise projections have been found to be alarming (i.e., [18–20]).

For these reasons, sandy shorelines have been the target of numerous interdisciplinary studies, which usually deal separately with their inshore or onshore/nearshore parts. Inshore studies aim to map bathymetry, morphology and marine habitats that are crucial for biodiversity and ecological processes [21], whilst onshore/nearshore studies mostly focus on coastal morphodynamics and the design/assessment of artificial and/or natural-based solutions that must be adopted to prevent erosion and flooding [22–24].

However, these measures, for both natural disaster mitigation and adaptation to climate change, require advanced models/tools to assess the risk with the appropriate spatial resolution and accuracy. Numerical models of varying complexity are the main tools for the assessment of erosion/flood risk and the design of coastal protection and other structures. These models cover various aspects of wave propagation, hydro-morphodynamics (coastal morphological evolution) and sediment dynamics at different scales and at different levels of detail (i.e., [24–27]). Yet, there is growing discussion on the sensitivity of these models and their outputs to the geomorphological, sedimentological, ecological and hydrodynamic data used to set up and to drive them. The flexibility and validity of these models are considered essential requirements, since they should be adaptable to a wide range of project designs and perform satisfactorily in a wide range of environmental conditions. Uneven seabed relief (i.e., hardgrounds, reefs), diverse sediment texture and the presence of particular habitats (i.e., seagrass) are important, as they modify the seabed friction during wave propagation, resulting in significant wave energy attenuation, changes in nearshore currents and potentially improved coastal protection (i.e., [28–30]).

As beach dynamics depend on the evolution of the entire sediment store, information on the topo-bathymetry, morphology, habitats and sediments of both inshore and the onshore parts of a beach is required for an appropriate assessment. These studies, though sometimes different in purpose, often employ common techniques, based on satellite imagery, unmanned aerial vehicles (UAVs) and topographic mapping/support [31]. Terrestrial measurements are obtained using Global Navigation Satellite System (GNSS) and terrestrial laser scanners (TLS), especially along high and irregular reliefs, whilst bathymetry and seabed morphology and habitats are mapped utilizing satellite and aerial (UAV) remote sensing techniques and marine hydroacoustics. Satellite imagery is used, among others, to study shoreline shifts and measure beach dimensions (usually through repeated satellite captures) [32,33] but also to identify/map seabed habitats [21,34] and estimate the nearshore bathymetry [35–37], usually at large spatial scales. UAVs provide high-resolution information, albeit on smaller spatial scales when considered in relation to satellites. This information is useful for the extraction of beach elevation, shoreline position and volumetric estimations [38] but can also be used (depending on the camera used) for habitat mapping in greater detail than that derived from satellites [39] and support bathymetric estimations [40]. Since UAV-based surveys achieve higher spatial resolution, they can calibrate/validate satellite-based assessments, although mostly over smaller spatial scales [39,41].

Real-time kinematic positioning (RTK) GNSS systems are employed for precise positioning during inshore [42] and onshore surveys and they also provide accurate elevation measurements during monitoring projects [43]. TLSs are nowadays routinely used for surveying sea cliffs [44], since they can provide accurate information at a relatively low cost, along steep and irregular coastal terrains where other remote sensing techniques underperform. The value of high-resolution TLS measurements has been demonstrated in numerous applications involving beach morphodynamics, surf zone wave transformation and wave runup studies, as well as in very shallow-water bathymetric surveying [45–50].

Even if remote sensing is considered effective in mapping habitats in water depths going down to ~50 m [51–53], its accuracy has been debated [54,55], especially in deeper waters. In comparison, hydroacoustic techniques provide high-quality geospatial data for bathymetry, habitats and sediment types. Traditionally, seabed habitat mapping has been based on side scan sonar and multibeam echo-sounder imagery, which are vessel-based marine remote sensing techniques [21,56]. Validation of this remotely sensed acoustic information is commonly provided by ground-truthing, which employs drop and towed cameras, remote operated vehicles (ROV) and grab sampling [57]. These techniques provide full coverage of the coastal area by high-resolution data and can calibrate/validate other remote sensing observations (from satellites and UAVs). Although the value of Multibeam echosounder (MBES) mapping is indisputable, technical and logistic limitations prevent data collection in water depths less than 5–10 m, where single-beam echo-sounders in a dense survey line network can provide high resolution bathymetric information [42] and/or habitat type characteristics [57].

Previous coastal surveys have been individually devoted to the study of beach morphodynamics or bathymetric and habitat mapping, often using similar remote sensing and ground-truthing techniques [21,39,45,53,58]. These studies have addressed some of the challenges in coastal mapping using either single-sensor approaches or combined remote sensing techniques to test and improve accuracy. The objective of this study was to use and integrate a multi-sensor approach in order to inter-validate the accuracy of their results, bridge methodologies with different scope and provide more detailed and accurate coastal information than those assessments based on single-sensor techniques. It aims to provide a holistic high-resolution approach for the observation of coastal geomorphology,

bathymetry and marine habitat distribution using modular inter-validations of different remote sensing techniques (satellites, UAVs and hydroacoustics) and ground-truthing information (underwater camera images and sediment sampling). Such observations form fundamental inputs for all tools/approaches used for the diagnosis, prognosis and management of beach dynamics and changing climate induced coastal hazards. This approach was tested/implemented in a microtidal, ‘pocket’ island beach in Cyprus (Eastern Mediterranean).

2. Study Area

The study site was selected in the framework of an “INTERREG V-A Greece-Cyprus 2014–2020” project (BEACHTECH), aiming to provide a structured approach for the assessment of the beach erosion risk in the North Aegean Islands and Cyprus under different sea-level rise scenarios and to design effective and cost-efficient technical responses for selected beaches. In Cyprus, a major tourist destination in the Eastern Mediterranean due to its almost year-round sunny weather and diverse landscapes, the pilot study area was Coral Bay, in the Municipality of Akamas (Figure 1).



Figure 1. Coral Bay in the municipality of Akamas, Paphos, Cyprus.

Coral Bay, one of the most touristic beaches in western Cyprus [19], is a typical microtidal pocket beach with a length of about 650 m and a width of a 20–35 m, bounded by two promontories that form steep sea cliffs. A much smaller, cliff-fronting beach (~80 m in length, max width of ~10 m) is located to the south of the main beach, at the northern side of the southern promontory (Figure 1). The microtidal Coral Bay has a southwestern orientation and is open to waves from the southwestern sector. The local authorities have reported beach erosion occurring during energetic weather events, with

the erosion being more profound at the northwestern beach stretch, whereas the central and southeastern sectors of the main beach have shown significant periodic fluctuations in width. The sea cliff of the southern promontory has also experienced erosion through wave undercutting. Since this cliff hosts overhanging residential properties, protection works have been constructed at its toe. Despite these works, small slope instabilities have been occasionally observed. Thus, the sea cliff has been the object of a TLS survey [59]. Hydrodynamic measurements during the most energetic winter period, in the context of an earlier local survey [38], showed significant wave heights (H_s) and maximum wave heights of 2.8 and 4.7 m, respectively, from a wave recorder deployed in 12.5 m water depth, whilst nearshore currents reached 0.3 m/s.

The wider coastal area comprises Pleistocene terrestrial deposits consisting of sandstones, sand, gravels and Holocene loose alluvial deposits (gravels, sands, silt, and clay). Although these materials are prone to erosion and transport to the coast, they cannot reach/enter Coral Bay due to its long bounding promontories; thus, Coral Bay forms a single sedimentary cell with no sediment exchanges with its neighbors. Also, the hydrographic network is very poor, with negligible intermittent flows that only sporadically delivers fluvial material.

A previous study [19] has found evidence of an erosional trend in the period 2010–2022, as well as significant exposure to erosion due to the mean and extreme sea levels projected under climate change; for example, the median projections of the morphodynamic model ensemble used in the study showed that by 2050 (Representative Concentration Pathway 4.5—RCP4.5), the maximum width of the beach will decrease between 9 and 32% and 88 and 93% under the mean sea level rise and the 1-in-50-years extreme storm event, respectively.

All the above imply that this highly touristic beach is susceptible to sediment losses that cannot be balanced by new sediments for the beach to remain stable. This is particularly worrying in the light of its high erosion risk projected under climate change. For those reasons, it was evident that a detailed geomorphological survey and monitoring of Coral Bay was a pre-requisite to help assess the future of the beach.

3. Methodology

The methodological framework of this study employs a multidisciplinary remote sensing approach to evaluate coastal geomorphology and marine habitats that combines terrestrial, aerial, satellite, and hydroacoustic data acquisition techniques, which also facilitate comparisons between areas of simultaneous coverage (Figure 2).

Onshore data acquisition involved GNSS and TLS surveys to gather detailed topographic information, as well as UAV surveys using RGB and multispectral sensors along with radiometric measurements for surface analysis and mapping. In the inshore part hydroacoustic surveys were carried out to obtain bathymetry, morphology and habitats, while PlanetScope and Sentinel 2 satellite data were also utilized for Satellite Derived Bathymetry (SDB) and habitat mapping. Drop camera and surficial sediment sampling were employed for ground-truthing of the remote sensing data.

The data collected underwent several processing steps (Figure 2). Pre-processing, including recording, masking, alignment, and noise removal, was conducted to prepare the data for analysis. The image-processing phase involved the generation of dense point clouds from the UAV data, the production of Digital Elevation Models (DEMs) and the calculation of the normalized difference water index (NDWI) from multi-spectral data to demarcate the land/sea boundary, i.e., the shoreline. In addition, sun-glint correction and ratio transformation algorithms were applied to the satellite images to estimate SDB. Hydro-acoustic data were processed to produce bathymetric and morphological maps focusing on the classification of underwater habitats.

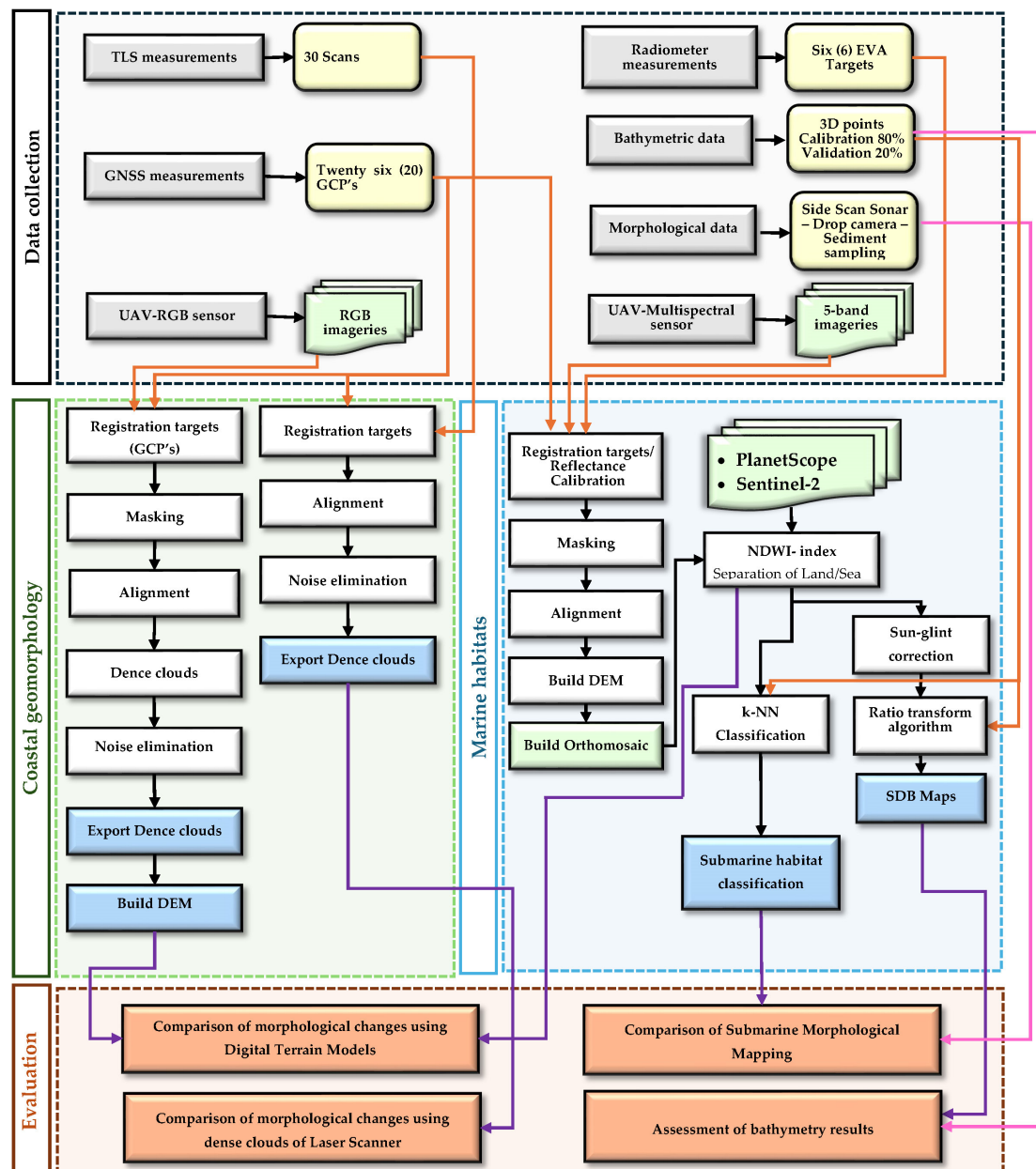


Figure 2. Workflow processing steps for mapping coastal geomorphology and marine habitats.

The evaluation phase involved a comparative analysis of changes in onshore and submarine morphology. The former was assessed by comparing dense point clouds and DEMs obtained from TLS and UAV imagery, allowing for the quantification of elevation changes over time. The latter involved evaluation of bathymetric models derived from SDB maps and hydroacoustic surveys to ensure spatial accuracy, while also validating bathymetric estimates with in situ measurements. A more comprehensive commentary and description of the aforementioned steps is provided in the subsequent paragraphs.

3.1. Data Collection

3.1.1. In Situ Survey Measurements

In the upper (landward) boundary of the beach, the shoreline and several vertical sections were mapped using a Leica Viva GS15 GNSS geodetic receiver (Leica Geosystems AG, Heerbrugg, Switzerland). The measurements transformed in the Cyprus Geodetic Reference System (CGRS93) to accurately define the beach's extent. These in situ measurements

were conducted at three (3) different temporal periods: on 2 June 2022, on 6 December 2022, and on 26 April 2023. In addition, twenty (20) Ground Control Points (GCPs) were fixed to assist in the post-processing of UAV data, along with seven (7) ground-based laser scanner waypoints for georeferencing the TLS point clouds.

Two topographic surveys using Leica's ground-based TLS ScanStation C10 (Leica Geosystems AG, Heerbrugg, Switzerland) took place on 2 June 2022, and on 26 April 2023. The TLS utilizes a pulsed laser, namely time-of-flight technology, which employs a green class 3R laser. The precision of the measurement is 6 mm and 4 mm in position over a range of 1 to 50 m, with an angular resolution of 60 mrad. The diameter of the laser dot is 4.5 mm at 50 m, with a scan rate of 50,000 points per second, a minimum focus of no more than 1 m, and a range of up to 300 m. Also, the TLS has a digital camera that can record and colorize the point clouds.

TLS mapping was carried out in a small segment of the sea cliff at the inner side of the southern promontory of Coral Bay (Figure 3). Here, the cliff has complex relief and steep slopes showing active erosion despite the rip-rap protection structure at its toe (Figure 3c). The cliff has a height of up to 17 m with some unevenly distributed vegetation, found in its upper slope. Comparing different dated DEMs produced by the UAVs was not feasible due to the complex and almost vertical sea cliff. Thirteen scans were carried out on 2 June 2022, followed by fifteen more scans on 26 April 2023; these resulted in the collection of a total of 600 million points. During the field measurements, a twin-targeted pole was used at waypoints with known coordinates for the georeferencing of the scans. It is noted that no TLS measurements were possible at the highest area of the cliff due to accessibility issues; in this region, there are gaps in the final point clouds.



Figure 3. (a) The study area with TLS (red box), (b) TLS—Leica Scanstation C10, (c) frontal view of the sea cliff at Coral Beach, (d) detachment surfaces and debris cones at the cliff toe.

3.1.2. Bathymetry and Submarine Morphology

Bathymetric data acquisition was conducted utilizing a high frequency hydrographic SonarMite v5 (Ohmex Ltd., Hampshire, UK) Single-Beam Echo Sounder (SBES), with a 0.025 m depth accuracy, which was paired with the TopCon Hiper HR RTK GNSS (~0.5 m accuracy) assembled on a 6 m inflatable boat. A Humminbird Helix 10 (Humminbird, Johnson Outdoors Inc., Eufaula, AL, USA) multi-parametric sonar was employed to map seabed morphology and habitats. The sonar utilizes CHIRP 2D technology and can capture simultaneously both the seafloor morphology (operating in a side scan sonar (SSS) mode—455 kHz) and the bathymetry (180–240 kHz). The system is versatile for a wide range of depths but is particularly effective in shallow waters. A dense grid of parallel and perpendicular lines was surveyed ensuring full SSS coverage of the seabed. For the very shallow water bathymetry (from the shoreline to 1.5 m water depth) the TopCon RTK GNSS was used. Ground-truthing of the SSS information was provided by using a drop Go-Pro 4K camera (GoPro Inc., San Mateo, CA, USA) at 28 locations, whereas a van Veen grab was utilized for the collection of 16 surficial sediment samples at locations selected following a preliminary sonograph interpretation.

3.1.3. Unmanned Aerial Vehicles (UAV)

UAVs are now widely used for the detailed topographic studies [60,61]. Two UAVs were employed for this study: (a) the DJI Phantom 4 RTK (DJI P4RTK), equipped with an RGB sensor and a camera resolution of 20 megapixels, enabling the generation of a highly detailed digital terrain model and (b) the DJI Phantom 4 Multispectral (DJIP4M), equipped with six integrated sensors (one RGB and five multispectral monochromatic sensors). Each sensor utilizes 2.08 megapixels. The spectral sensitivity of the sensors allows for the capture of light within the following wavelength ranges: blue (450 ± 16 nm), green (560 ± 16 nm), red (650 ± 16 nm), red edge (730 ± 16 nm) and near-infrared (840 ± 26 nm). The field of view (FOV) of the lenses employed is 62.7° . Additionally, the UAV utilizes a built-in spectral sunlight sensor to capture solar radiation.

A total of six drone flights were undertaken at an altitude of 100 m. The flights included three DJIP4RTK sensor flights and three DJIP4M flights on the same date (2 June 2022, 6 December 2022, 26 April 2023). The DJIP4M flight was carried out concurrently with the bathymetric survey. In order to obtain the requisite data, a different flight pattern was employed in each survey. This was due to the fact that flights conducted with the RGB sensor were focused primarily on the coastline, whereas flights conducted with the multispectral receivers were focused on the entire study area.

For the UAV survey, it was crucial to conduct measurements with a GNSS receiver to ensure accurate georeferencing of the final product, as noted. Furthermore, the processing of the multispectral sensor images necessitated additional field measurements using the SVC-1040 spectroradiometer (Spectra Vista Corporation, Poughkeepsie, NY, USA) for calibration purposes. The SVC-1040 spectroradiometer had a spectral range of 350–2500 nm. The front optical lenses used had a field of view of 4° and all data were collected from a height of 1.1 m, corresponding to a circular ground plane with a diameter of 0.08 m. The instrument uses three detectors covering the visible, near-infrared, and shortwave infrared with bandwidths: ≤ 3.5 nm for 350–1000 nm, ≤ 3.8 nm for 1000–1885 nm, and ≤ 2.5 nm for 1885–2500 nm. Measurements were made between 10:00 and 14:00 local time.

During the UAV flights, measurements of Lambertian targets and Ethylene Vinyl Acetate (EVA) foam panels were collected simultaneously to ensure accurate calibration and validation of the multispectral data. The Lambertian surface offers the highest diffuse reflectance among all known coatings in the ultraviolet, visible, and near-infrared regions of the electromagnetic spectrum. Specifically, its reflectance surpasses 99% in the 400–1500 nm

range and exceeds 95% in the 250–2500 nm range [62]. EVA foam panels were utilized due to their high Lambertian behavior [63,64], but also a high horizontal homogeneity [65]. The dimensions of each EVA foam panel used in the study were 0.30 m (length) \times 0.30 m (width) \times 0.01 m (thickness). The colors of the EVA foam used were black, grey, and white. These panels are very convenient as they are light, easy to carry, and easy to clean with compressed air. They are useful materials for reflection reporting in calibrating UAV images and radiometric measurements [66]. More specifically, three EVA foam targets and one Lambertian surface were positioned on the eastern side of the beach, while one Lambertian surface and three additional EVA foam targets were placed near the central part of the beach. Measurements were taken as the UAV flew directly above these targets, ensuring consistent observation angles and minimizing potential discrepancies due to variations in lighting conditions. A total of twelve measurements were recorded for each target to enhance statistical robustness and reduce uncertainties. Additionally, a radiometric calibration was conducted using the Lambertian reference surface to standardize reflectance values, ensuring the accuracy of subsequent multispectral analyses [62]. Since the spectroradiometer operates as a hyperspectral device while the UAV functions as a multispectral one, it is essential to perform band adjustments to correlate the datasets generated by these two distinct techniques and devices. The DJIP4M generates Digital Number (DN) values, which are then converted into reflectivity values during image processing using DJI TERRA software v.3.5. This conversion leverages the values from the Spectral Sunlight Sensor and a reference reflectance value for each band validated by radiometer measurements. To derive the mean spectral reflectance from the spectroradiometric measurements for each UAV sensor (i.e., for each band), it is crucial to reference the Relative Spectral Response (RSR) filter graph corresponding to the UAV multispectral sensor (Figure 4). In addition to the spectroradiometer measurements, mainly for calibrating UAV data, a calibrated Spectralon panel—Lambertian surface and EVA foam were used [67,68].

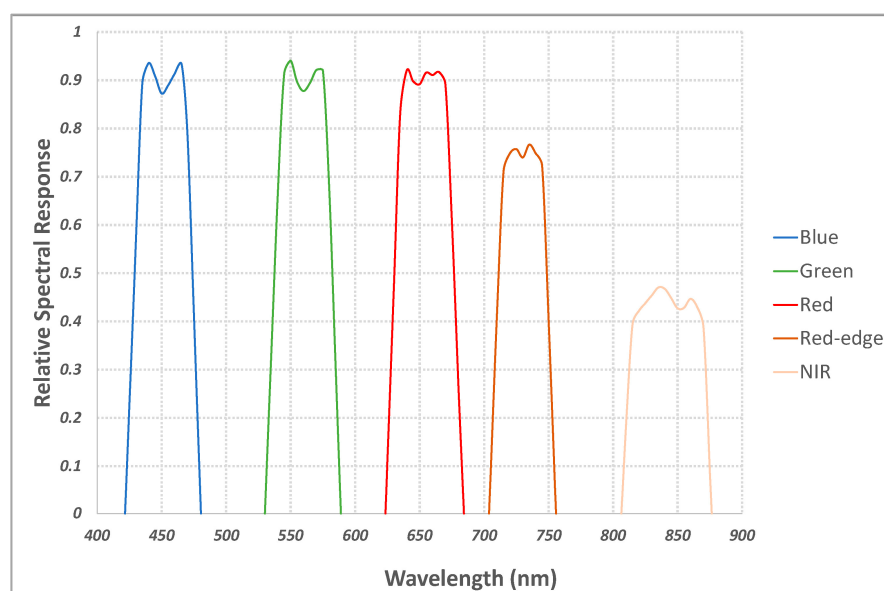


Figure 4. Relative Spectral Response of DJIP4M.

Equation (1) was used to calculate the representative reflection value of the UAV's camera bands.

$$r_{x,k} = \frac{\int_{425}^{875} R_x(\lambda) C_k(\lambda) d\lambda}{\int_{425}^{875} C_k(\lambda) d\lambda} \quad (1)$$

where $r_{x,k}$ = average spectral value of the calibration matrix x and the k band; λ = wavelength (nm); x = surface area variation for the range from 425 to 875 nm of the calibration/validation matrix x ; and C_k = relative spectral sensitivity of the k band for the DJIP4M sensor in the range from 425 to 875 nm.

3.1.4. Satellite Data

In order to monitor the shoreline position, estimate the bathymetry and delineate marine habitats, three PlanetScope and one Sentinel-2 satellite images of different resolutions were also used. The PlanetScope and Sentinel-2 satellite images were acquired, georectified, and radiometric and atmospheric corrected to enhance data accuracy. Furthermore, the Sentinel-2 image was resampled using a reference band with a 10 m spatial resolution within the Sentinel Application Platform (SNAP) software v7.0. The dates of the images were selected to be the same with the other (in situ) measurements to allow data comparisons (Table 1).

Table 1. Details of optical satellite imagery.

A/A	Satellite	Product Name	Resolution (m)	Date Acquisition	Sensing Time	Cloud Coverage %
1	PlanetScope	02062022_Coral_psscene_analytic_8b_sr_udm2	3	2 June 2022	07:38	0.00
2	PlanetScope	06122022_Coral_psscene_analytic_8b_sr_udm2	3	6 December 2022	07:38	14
3	PlanetScope	20230425_074318_43_24ab_3B_AnalyticMS_SR_8b_clip	3	25 April 2023	07:43	3.47
4	Sentinel 2	S2A_MSIL2A_20230426T083601_N0509_R064_T36SVD_20230426T130804	10	26 April 2023	08:36	40.49

PlanetScope's multispectral images have eight bands with 3 m resolution (Coastal Blue, Blue, Green i, Green, Yellow, Red, Red Edge, NIR). The Sentinel 2 medium-resolution multispectral images have 12 spectral bands with three different resolutions (bands/resolution: Coastal blue/60 m, Blue/10 m, Green_i/10 m, Green/10 m, Red/10 m, Vegetation Red Edge/20 m, Vegetation Red Edge/20 m, Vegetation Red Edge/20 m, NIR/10 m, Vegetation Red Edge/20 m, Water vapor/60 m, SWIR/60 m, SWIR/60 m, SWIR/60 m).

3.2. Processing

3.2.1. Onshore Geomorphology

The GCPs collected using the RTK GNSS receiver were used in the processing of the aerial photography images, as well as for mapping the shoreline and the beach dimensions. The data collected were stored in appropriate file formats to enable efficient processing and imported into a Geographic Information System (GIS) environment. This facilitated the generation of characteristic profiles and shoreline change comparisons to define areas of beach erosion or accretion.

UAV surveys helped to gain further information of the beach morphology. The Structure-from-Motion (SfM) photogrammetric technique has been implemented in this study, generating two-dimensional and three-dimensional representations from sequences of two-dimensional images. The SfM approach operates on the same fundamental principles as stereoscopic photogrammetry and can be determined from a collection of overlapping shifted images. This technique is regarded as one of the most efficient methods in computer vision, consisting of a set of algorithms that identify shared features in images and transform them into three-dimensional data [69]. It has demonstrated both efficiency and reliability, providing a high level of accuracy. Moreover, this technique provides a cost-effective alternative to traditional surveying methods, including TLS, GNSS surveys, and LiDAR [70,71].

The data obtained from DJIP4RTK were then analyzed for all three acquisition dates using the Agisoft Metashape software v 1.8.5 [72]. UAV flights utilizing the RGB sensor were employed to produce high resolution DEMs and orthophotos. The subsequent processing steps involved importing the images and creating masks to isolate specific areas, which were excluded from processing. All GPS field measurements were then integrated into the software by correlating them with the identifiable points in the images. Prior to generating the DEM, the point cloud underwent a classification process to eliminate any noise that could disrupt comparisons between data from two different dates. This process involved the removal of elements such as vegetation, umbrellas, sunbeds, people, etc., ensuring that the resulting point cloud accurately reflected the ground points. The final stage of the process was to extract a DEM using the dense cloud and DEM data to generate an orthophoto of the study area. Subsequently, the results were imported into ArcGIS Pro [73], where a comparative analysis of the elevation discrepancies among the three DEMs was conducted, alongside with the shoreline digitization. In addition, elevation profiles were produced and visualized using the results from the UAV, in order to study topographic features. This was achieved by developing cross sections in AutoCAD Civil 3D. Such methods are widely used in coastal and environmental studies to monitor soil changes, assess erosion or evaluate anthropogenic impacts [74–76]. The analysis of temporal changes through comparisons of data collected at multiple intervals enables the assessment of terrain stability and the identification of significant geomorphological transformations.

Finally, the TLS data were used to investigate potential sediment micro-movements indicating erosion or areas of deposition at the sea cliff of the inner side of the southern Coral Bay promontory (Figure 1); two high-accuracy point clouds spanning almost 15 months were created and compared. Although TLS mapping was restricted in a small segment of the cliff, this effort constituted a challenging task due to cliff relief complexities and accessibility issues. The data obtained amounted to approximately 8 gigabytes due to the high spatial resolution (accuracy in the order of millimeters). The first step of data processing was performed using Leica's Cyclone software v 2021.1.2 [77] and involved aligning and merging the point clouds to create a unified point cloud, utilizing the measured targets to assist the georeferencing and alignment processes. Noise filtering revealed that the most significant problems in both scans were produced along the small beach fronting the cliff and particularly in regions with wave activity. The Root Mean Square Error (RMSE) of the final point cloud on the first scan was calculated as 0.010 m, whilst that of the second scan as 0.009 m. The second step of the processing procedure involved point cloud comparisons of the two different scans using the CloudCompare software v2.12.4 [78] and the Multiscale Model to Model Cloud Comparison (M3C2) algorithm [79]. This algorithm calculates the measurement of the orthogonal distance between two-point clouds, and the standard deviation of the change from the point clouds can be used to estimate a true change confidence interval. Thus, the final point cloud shows the surface changes relative to the first point cloud. In the end, the analysis of two-dimensional sections derived from the two point clouds was conducted using AutoCAD Civil 3D software 2018 [80]. Three areas were selected for the creation of sections to demonstrate the morphological changes observed in the study area through the utilization of the TLS.

3.2.2. Bathymetry and Submarine Morphology

Bathymetric data processing involved the removal of measurements that introduced significant errors in relation to the neighboring points and consequently to the bathymetric map. All measurements were georeferenced in the WGS84 Universal Geodetic Reference System, utilizing the UTM Transverse Mercator Projection. The processed files were

imported into a GIS environment, where point data were transformed into continuous surface information through linear interpolation methods.

The SSS data were first converted into .xtf files, which were then imported into Sonarwiz software v.8.0, allowing for post-processing, analysis and mosaicking of the sonographs. Processing initially involved automatic bottom tracking (occasionally manually), which allows for water column removal and production of isometric records and then gain adjustments and de-stripe and nadir filtering to better capture various features. The synthesis of overlapping records led to the creation of a high resolution georeferenced (GeoTIFF) mosaic of high resolution (0.25 m), which was subsequently imported into a GIS environment. Further examination of both the individual SSS records and the mosaic revealed different reflectivity tones that aided in the construction of the morphological map of the study area. The collected sediment samples were analyzed in the laboratory by dry sieving (set of -2 to 4ϕ screens, at 1ϕ interval) due to the coarse sediment texture, following the procedure of Folk [81] and Blott and Pye [82] for the extraction of grain size statistical parameters. The combined analysis of the mosaic with the ground-truthing information from the drop camera and sediment sampling, led to the identification of four reflectivity (R) types corresponding to specific substrate or habitat types.

UAVs and satellite data of varying resolutions were also utilized to estimate bathymetry, with many of the processing steps being similar for both methods. To generate an orthomosaic, however, additional processing steps were required for the UAV data. These were performed in Agisoft's Metashape software v 1.8.5 with a multi-spectral sensor closely resembling those used for aerial photography with an RGB sensor. More specifically, once the images were imported into the DJI Terra software v1.0, the user selected the images, created a mask on the black calibration EVA target, and input radiometer measurements at 1 nm intervals. The subsequent processing stages corresponded to those applied to RGB sensor images. These included importing GPS field measurements and correlating them with the image set, creating masks within the image set to remove noise, aligning the images, generating a DEM, and compiling a mosaic of the study area. It is important to highlight that before extracting the orthomosaic, an additional step was necessary; this is because the output bands of the generated orthomosaic contain 16-bit integer values. In this context, 100% reflectance in each band corresponds to the average value of that band, referred to as 32,768. To obtain the values of each channel, the Raster Calculator was employed to divide each band by the value of 32,768, representing the normalized reflectance within the range of 0 to 1.

To validate the orthomosaic reflectivity values and proceed with the bathymetry estimation, first it was necessary to correlate the radiometer measurements with all EVA targets. To this end, the orthomosaic was imported into a GIS environment, where polygons were created in the areas where the calibration targets were located. The average reflectivity values of these polygons were then extracted. Subsequently, the EVA reflectance measurements of the targets were calculated and converted to average spectral reflectance values using Equation (1) and the RSR of the sensor, as can be seen in Figure 4.

The next phase of the process entails estimating bathymetry by utilizing the generated orthomosaic, PlanetScope, and Sentinel 2 satellite images. The initial step in estimating bathymetry concerns the delineation of the shoreline using the NDWI (Equation (2)). This approach facilitates the detection of water features in digital images captured by passive sensors [83]. After applying the NDWI index, it was necessary to identify the water/land boundary value. Using the Raster Calculator tool, land and sea masks were created. The segmentation of land and sea in each NDWI-derived raster image was performed by applying a threshold determined using the Otsu algorithm, implemented through the Iso Cluster Unsupervised Classification tool. This approach enabled the determination of an

optimal threshold, effectively minimizing intra-class variance and enhancing the accuracy of coastal boundary delineation.

$$NDWI = \frac{B_{green} - B_{NIR}}{B_{green} + B_{NIR}} \quad (2)$$

where B_{green} is the green band, and B_{NIR} correspond to the near-infrared radiation band values.

The next step involved applying a 3×3 median filter to reduce high-frequency noise, such as sun glint, followed by the ratio transformation method as outlined by Stumpf in 2003 [84]. The ratio transformation method offers several key advantages when using passive multispectral imagery for mapping shallow water bathymetry, compared to other available methods. The ratio transformation algorithm (Equation (3)) can be applied to bands with different absorption in water and to wavelengths of any sensor. Since the blue and green bands have lower absorption, the ratio of the two bands remains constant despite different bottom shading at a constant depth.

$$Z = m_0 \frac{\ln(n \times r_{rs}(li))}{\ln(n \times r_{rs}(lj))} - m_1 \quad (3)$$

where Z is the depth, m_0 and m_1 are constants for tuning the model to the actual depth, n is a constant to ensure that the ratio remains positive under all values, and $r_{rs}(li)$ and $r_{rs}(lj)$ are the bands in blue visible (li) and green (lj) light.

At this stage of the analysis, 80% of the field bathymetric data, consisting of 46,913 points, were used in Equation (3) to create a linear regression model. This model illustrates the relationship between the bathymetric points and the corresponding values generated by the equation, assisting in the estimation of bathymetry. To evaluate the accuracy of bathymetric results, two statistical parameters were considered: the correlation coefficient R^2 and the RMSE (Equation (4)), calculated using 20% of the remaining in situ bathymetric data (11,728 points).

$$RMSE = \sqrt{\sum_{j=1}^n \frac{(Z_B - Z_{ID})^2}{n}} \quad (4)$$

where n is the number of the field points, Z_B is the estimated bathymetry and Z_{ID} is the in situ depth data.

Finally, comparison of the results obtained from the SSS with those from the UAV and satellite sensors was carried out in order to extract and evaluate habitat distribution. To ensure that the data aligns with the date when the field data was collected, additional orthomosaic processing was performed. The k-nearest neighbors (k-NN) algorithm was employed for supervised classification using the orthomosaic generated by the DJIP4M UAV and the PlanetScope satellite imagery captured on the same date. The k-NN algorithm is a well-established and widely utilized tool in machine learning [85,86] first described by Fix and Hodges [87]. This algorithm classifies an image into specific feature regions based on sample data associated with predefined categories. The classifier's effectiveness depends on the Euclidean distance used to determine the nearest neighbors. When implementing k-NN, classes are created, and nearest neighbors are identified based on the classifier chosen by the user [86]. The orthomosaic was classified using ArcGIS Pro software 2.9, employing the NDWI index to effectively separate land and sea. A new shapefile was created with 100 points, which was correlated with the results from the SSS. This step used these points as calibration data for the k-NN classifier. The k-NN classifier was then implemented within ArcGIS Pro, with the classifier parameter set to 5. Upon executing the algorithm on

the images, classification results were obtained. To assess the classification results, 1000 random spatial accuracy evaluation points were generated to ensure a statistically valid sample for validation. The results from the SSS were used as ground truth. A confusion matrix was then created to evaluate the classification accuracy across the three specified substrate types. The confusion matrix provided metrics including producer accuracy, user accuracy, and the Kappa Agreement Index (KIA) as referred by Nababan et al., in 2021 [88]. The formulas to calculate the level of accuracy for Overall Accuracy (OA—Equation (5)), Producer (PA—Equation (6)), and User Accuracy (UA—Equation (7)) are as follows:

$$OA = \frac{\sum_{i=1}^k n_{ii}}{n} \quad (5)$$

$$PA_j = \frac{n_{jj}}{n_{cj}} \quad (6)$$

$$U_i = \frac{n_{ii}}{n_{ci}} \quad (7)$$

where n = number of observations, n_{ii} = number of observations in column i and row i , and n_{jj} = number of observations in column j and row j . n_{cj} = the number of samples classified into the category of j , n_{ci} = the number of samples classified into category i .

4. Results

4.1. Onshore Morphology

Coral Bay beach showed a varying morphology and width during the monitoring period. Its dynamics can be differentiated into two sections: the northwestern and the southwestern sections. The width of the beach varied alongshore, with the greater widths (almost 30 m) found in its southeastern part. The northwestern section appeared to be under erosion, with the beach showing in some areas a width of only 2 m. The photogrammetric analysis produced several products for further evaluation, including a DEM and an orthophoto of the study area. Comprehensive data processing and analysis resolved the distance errors observed in the alignment procedure (Table 2).

Table 2. RMSE of photogrammetric products.

A/A	Dates	X Error (cm)	Y Error (cm)	Z Error (cm)	XY Error (cm)	Total Error (cm)
1	2 June 2022	1.63	1.60	0.65	2.28	2.37
2	6 December 2022	2.23	2.98	0.95	3.72	3.84
3	26 April 2023	1.58	1.52	0.80	2.19	2.33

The results of the comparative analysis of the DEMs created for the three dates are presented in Figure 5, together with the digitized shorelines. The elevation differences for each of the two compared periods were found to decrease by as much as -0.6 m in the northwestern beach section, whereas in the southeastern section, increases of up to $+0.6$ m were recorded (Figure 5). Overall, beach elevation ranged from -1.1 to $+1.2$ m, appearing consistently lower to the northwest. During the first period (summer–autumn), the beach appeared relatively stable along its northwestern section and accretionary along its southeastern section (beach progradation locally up to 8 m). Interestingly, during the most energetic winter–spring period, the northwestern and most vulnerable section of the beach showed accretion (by up to 4.5 m), but also elevation decreases of up to 1.1 m (Figure 5). The southeastern beach section also showed accretion in this period (0.5–8.5 m).

In general, in relation to June observations, the beach showed increases from 1.5 to 14 m, during almost a year.

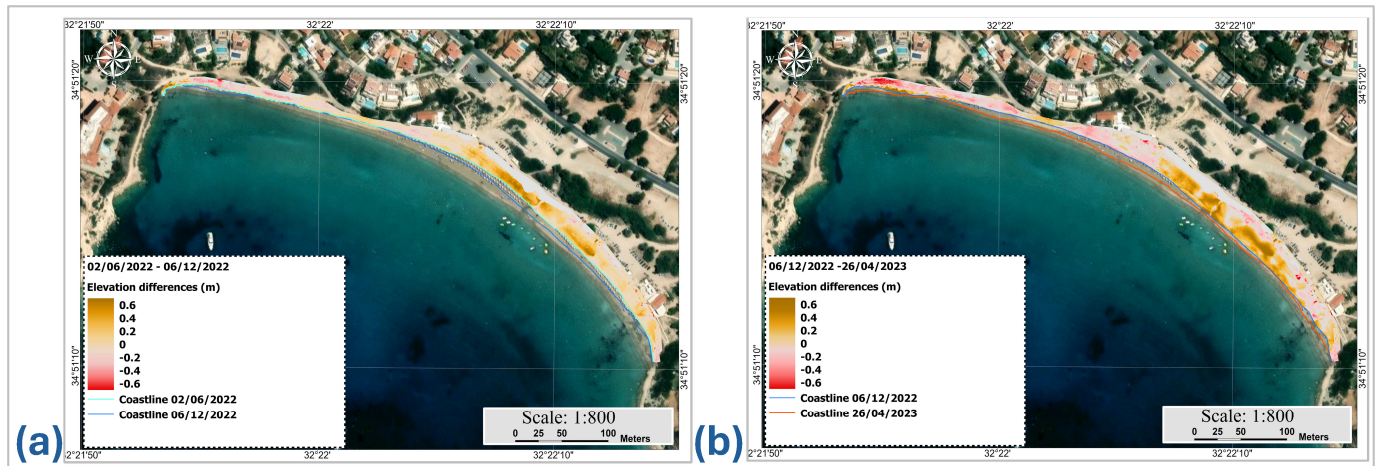


Figure 5. Elevation differences between DEMs: (a) 2 June 2022–6 December 2022, (b) 6 December 2022–26 April 2023.

Segmentation of the beach and creation of sections along the beach for the three available DEMs verified elevation changes over time, suggesting sediment losses or gains (Figure 6). Significant elevation variability was found along the northwestern segment of the beach (section A–B, Figure 6b). Elevation lowering was observed during the winter, whilst during spring, the beach recovered, and elevations locally exceeded the initial profile. Maximum elevation differences of 0.4–0.5 m were observed between 6 December 2022 and 26 April 2023 profiles. In the central beach segment (B–C, Figure 6c), the elevation showed small variability, with the highest recorded variation being 0.3 m. During the first period (2 June 2022–6 December 2022), the beach showed both sediment gains and losses, whereas in spring 2023, elevations appeared mostly restored. The southeastern beach segment (C–D, Figure 6d) showed notable elevation differences (up to 0.6 m) compared with the other two segments, especially along its northwestern section. More specifically, during winter 2022, elevations increased, whilst in spring 2023, the beach profile diminished, restoring equilibrium. For the easternmost part of section C–D, changes were minimal.

Moreover, a comparative analysis of shorelines derived from the DJIP4RTK data versus those obtained from PlanetScope satellite imagery was performed. The extraction of the UAV coastlines was achieved through visual interpretation due to the lack of multispectral data. Shoreline positions were also estimated from satellite imagery using the NDWI index [89,90] and were compared with those from the DJIP4RTK data in order to identify and evaluate potential discrepancies. Significant differences were found between the two datasets: shoreline deviations varied alongshore between 3.5 and 9.0 m in summer (Figure 7a), from 1.4 to 8.1 m in winter (Figure 7b), and between 1.3 and 14.0 m in spring (Figure 7c). Interestingly, the satellite derived shorelines were constantly located seaward of those estimated from UAV data and the highest deviations appeared at beach edges. The observed discrepancies might be attributed to various factors, such as differences in the data spatial resolution and accuracy, as well as time differences in the satellite and UAV image captures [91].

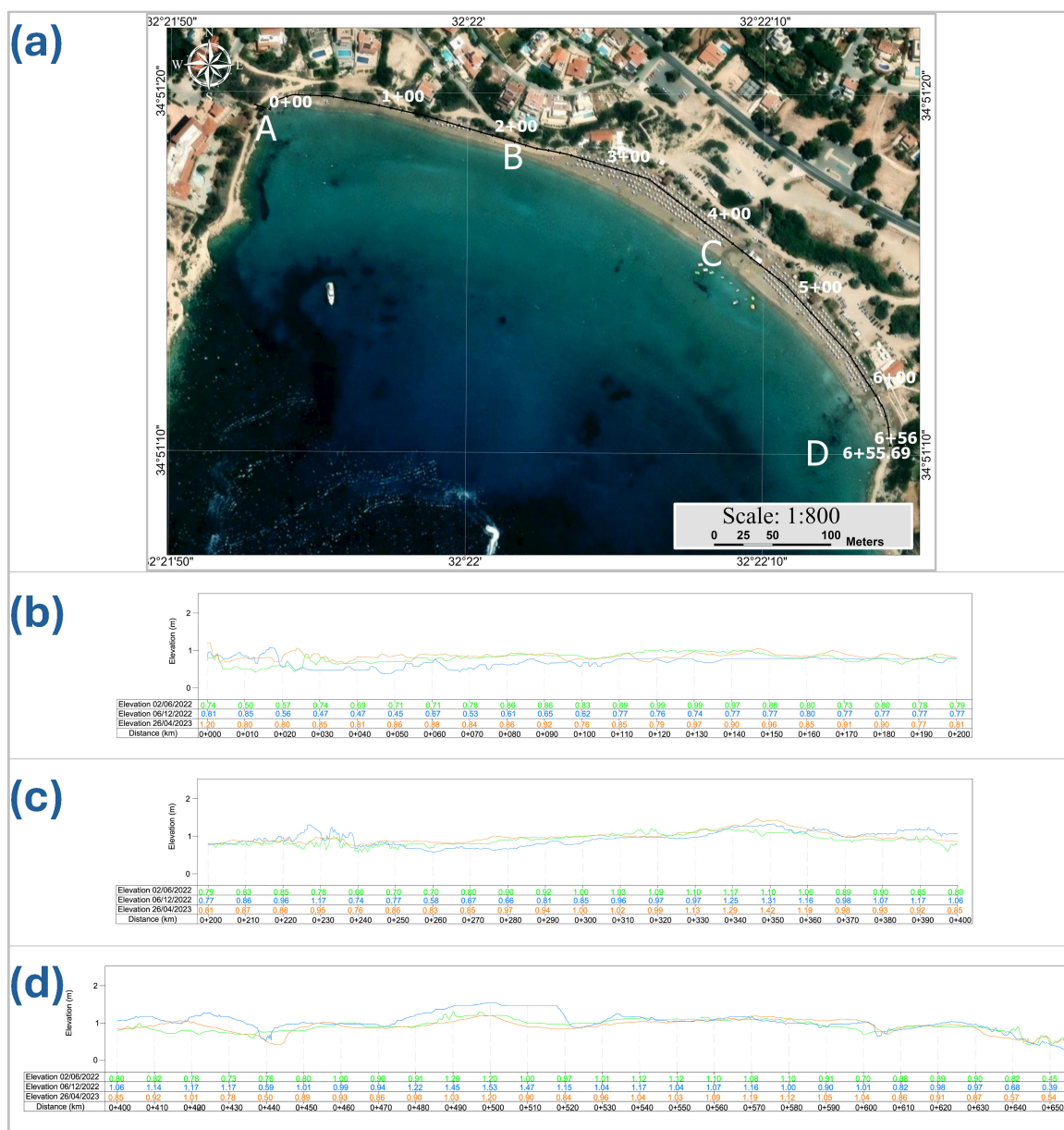


Figure 6. Comparisons of beach elevations along the Coral Bay beach from the DEMs produced by UAV scanning in 2 June 2022, 6 December 2022, 25 April 2023. (a) Stations—distance of the sections, (b) sections A–B, (c) sections B–C, (d) sections C–D.

The TLS was used to map the sea cliff found to the southeast of the Coral Bay beach and capture potential fine-scale morphological changes through the comparison of TLS point clouds from different times (Figure 8); topographic changes with blue and red colors represent positive and negative variations in distances, respectively, matching materials deposited or eroded. The most significant erosion (detachment surface) was identified on the eastern part of the slope, showing a change of up to 0.65 m, whereas on the western slope, smaller differences were recorded (up to 0.30 m). At the sea cliff's top, the results showed material deposition that was probably due to its vegetation growth, which potentially affected the reliability of the measurements.

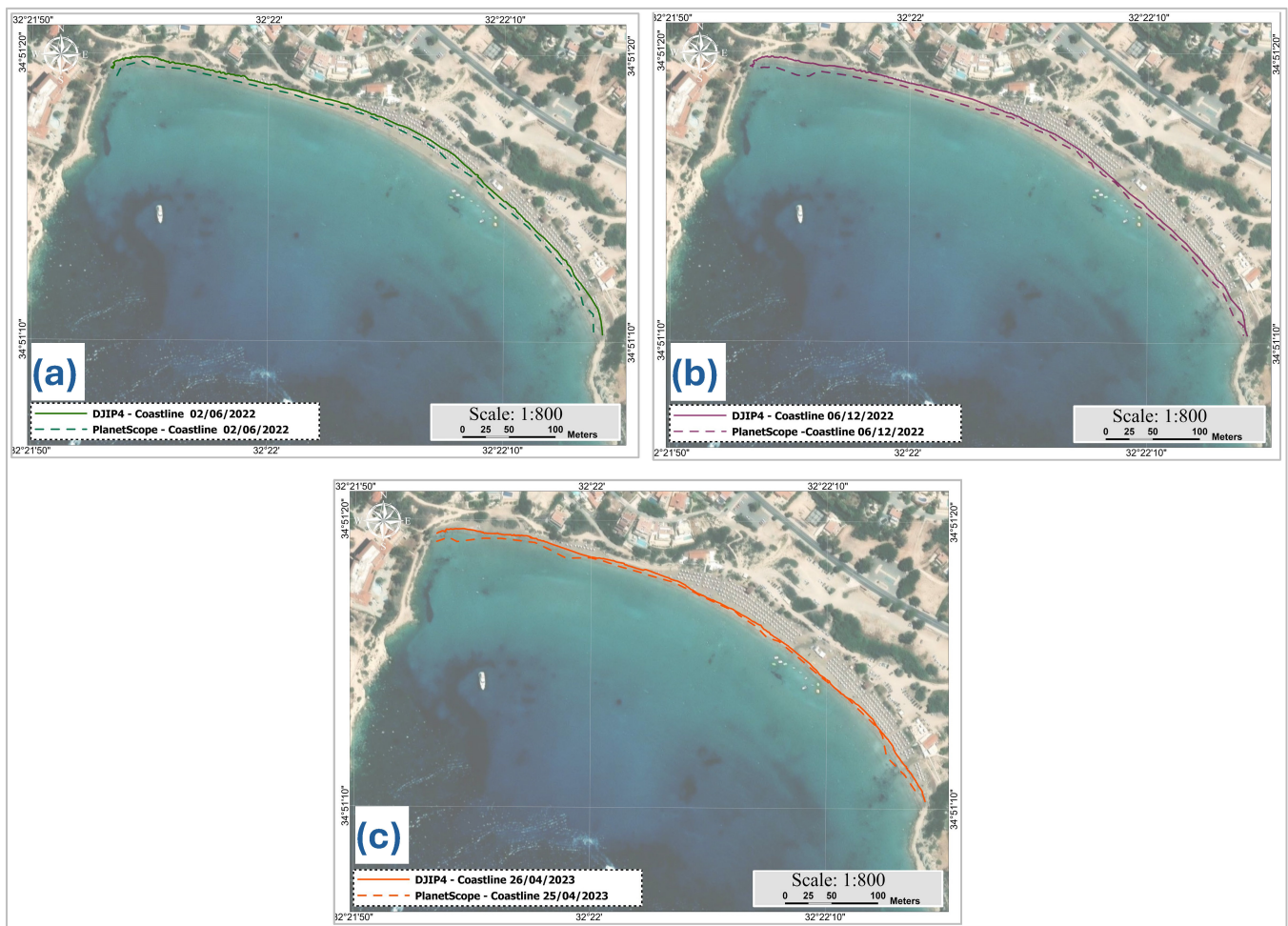


Figure 7. Coastline vectors extracted from DJIP4RTK and PlanetScope: (a) 2 June 2022, (b) 6 December 2022, (c) 26 April 2023.

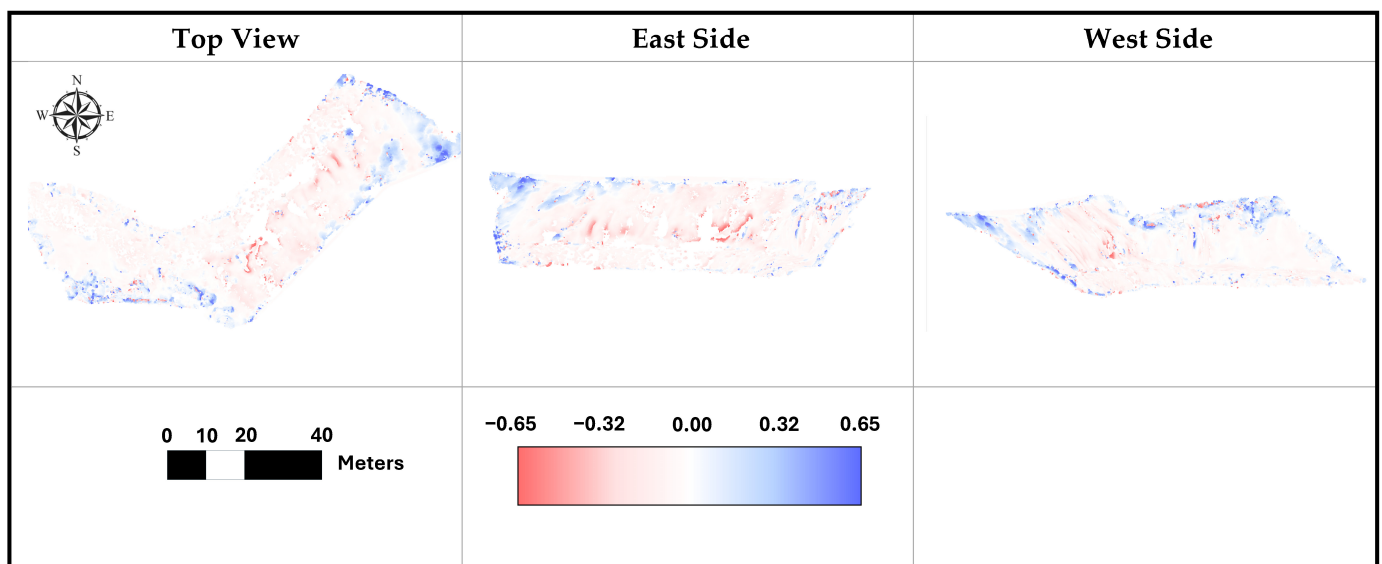


Figure 8. Temporal comparison of TLS point clouds using the M3C2 algorithm, focusing on the sea cliff of Coral Beach.

Comparisons along three cross sections of the sea cliff, generated from the collected point clouds, showed significant morphological changes in the 15-month span between the two surveys (Figure 9). In section A–A', the elevation increase from 8 to 11.5 m is primarily

attributed to vegetation overgrowth and cannot be safely evaluated. Cross section B–B' revealed significant cliff erosion between elevations of 3 and 10 m, without corresponding changes at the small beach fronting the cliff. In comparison, section C–C' showed a mostly stable profile; erosion was only discernible between elevations of 4 m and 7 m.

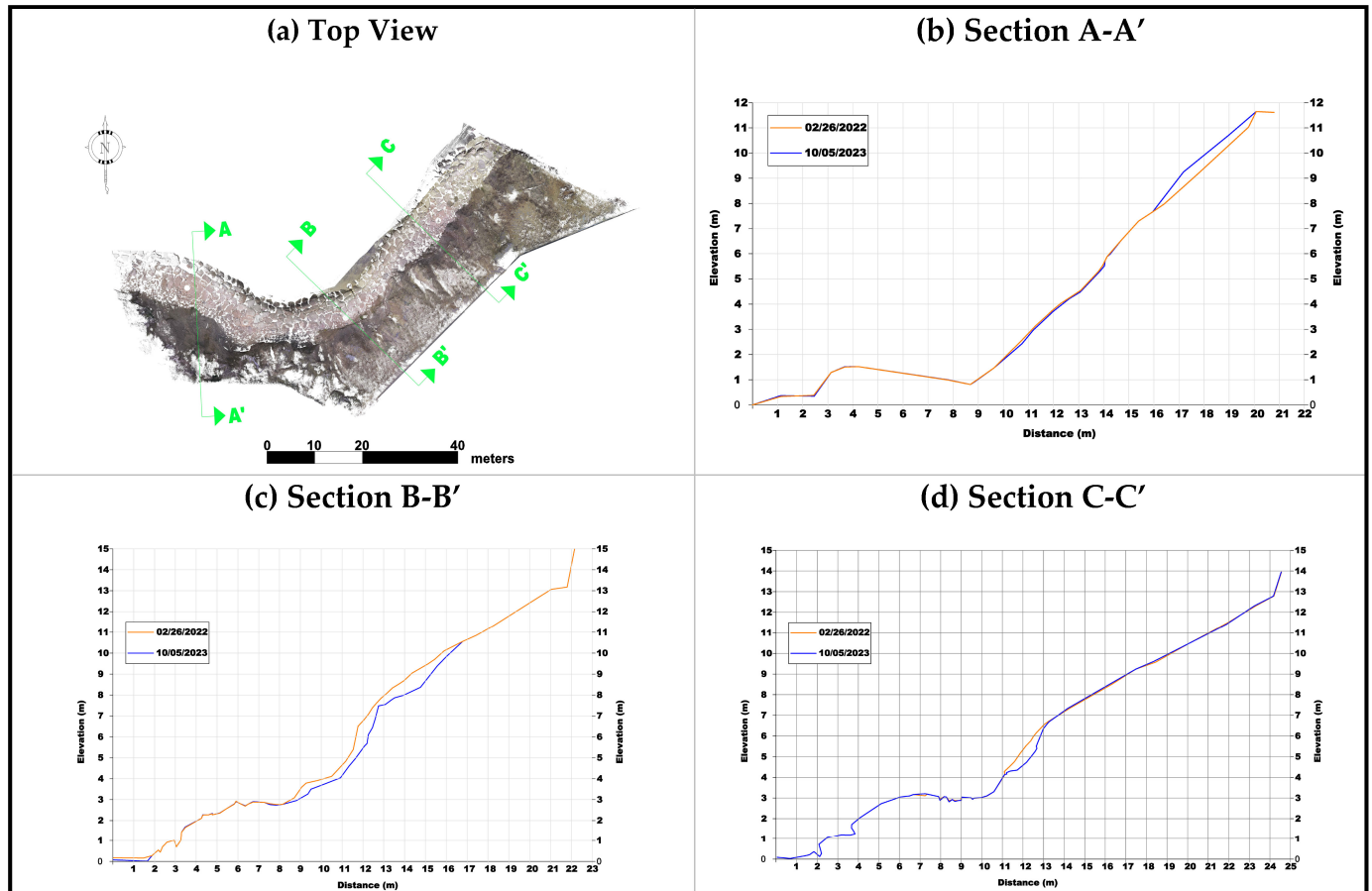


Figure 9. (a) Positions of cross sections across the sea cliff and (b–d) profile comparisons between the two survey periods.

4.2. Bathymetry and Submarine Morphology

The bathymetry and the seabed morphology and habitats in Coral Bay were mapped down to about 20 m water depth using hydroacoustic methods, ground-truthed by surficial sediment samples and drop camera images. However, processing and analysis of the satellite images and the UAV orthomosaics revealed that they could not produce reliable results deeper than 10–11 m water depth; thus, the appraisal of their skills to map accurately the seafloor was restricted to these depths.

The high-quality SBES data allowed for the creation of a detailed bathymetric map, which showed that the Coral Bay embayment can be differentiated into three zones with different characteristics. The most inshore zone, extending down to ~6–7 m in the central part of the surveyed area, is characterized by smooth morphology; seabed perturbations appear close to the promontories at both sides (Figure 10a). The middle zone extends down to about 16–17 m water depth, occupying the greater part of the surveyed area and exhibits uneven relief. Finally, the deeper zone is characterized by a very smooth relief.

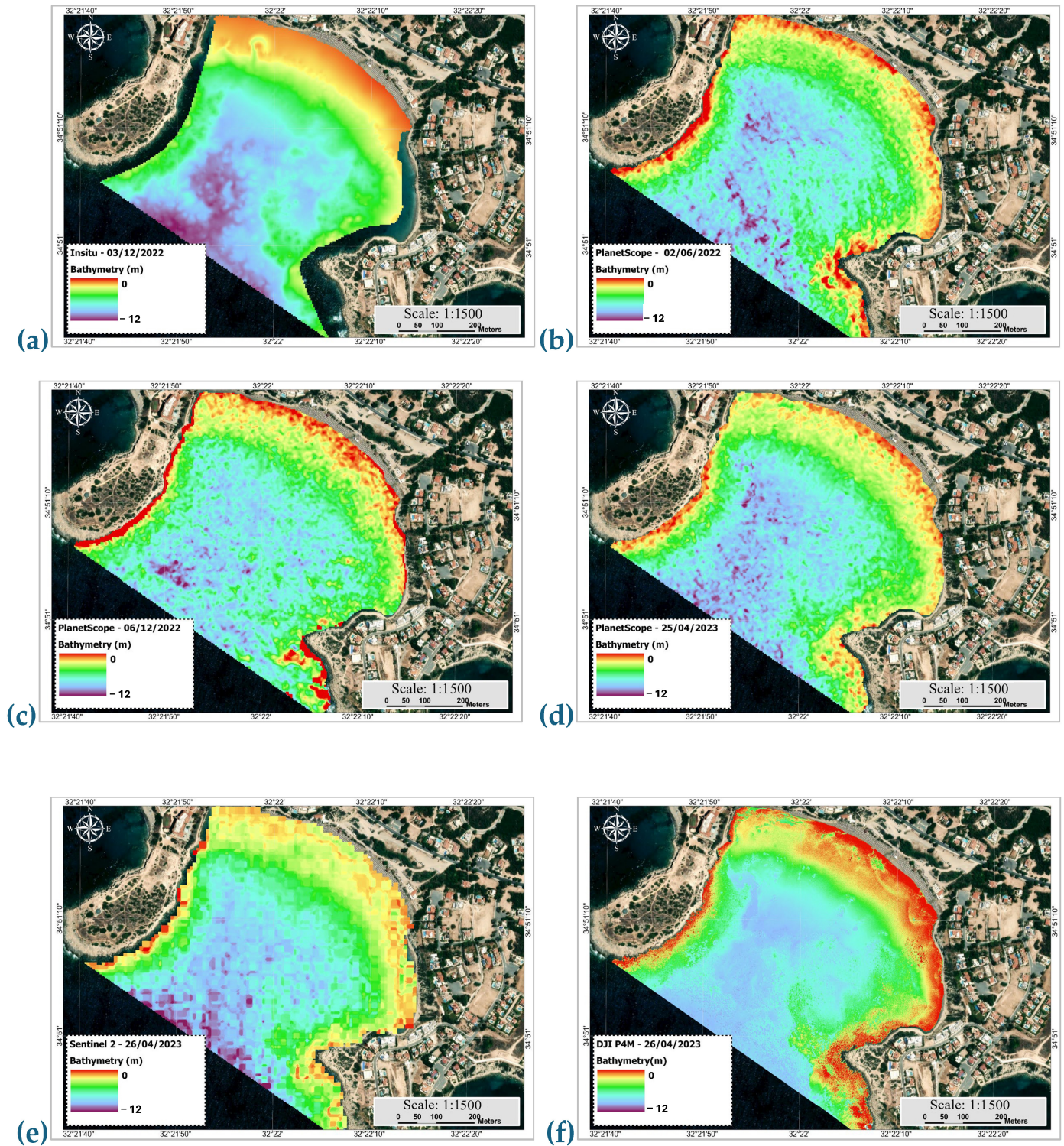


Figure 10. Coastal-derived bathymetry using (a) in situ SBES data collected on 3 December 2022; (b) PlanetScope image captured on 2 June 2022; (c) PlanetScope image captured on 6 December 2022; (d) PlanetScope image dated 25 April 2023; (e) Sentinel 2 images dated 26 April 2023; (f) DJIP4M images dated 26 April 2023.

Bathymetric estimations were attempted for all data sets of the DJIP4RTK and the DJIP4M. However, only one of the three DJIP4M analyses was successfully completed. A major issue was associated with the significant level of human activity in the study area during the 2 June 2022 survey that did not allow for the alignment of images to produce a comprehensive orthoimage. Also, the high cloud coverage observed during the

6 December 2022 survey resulted in a low correlation coefficient between the radiometer measurements and the values of the generated multispectral image. In contrast, the data analysis of the 26 April 2023 DJIP4M survey was successfully completed, resulting in a 0.05 m orthomosaic with an estimated range of the GCPs errors of $x = 4.41$ cm, $y = 5.88$ cm and $z = 1.03$ cm. The reflectivity of the orthomosaics across all bands was thoroughly validated, revealing a strong correlation with the fourteen field measurements taken with a spectroradiometer on the EVA targets. The correlation coefficients were 0.98 for the blue channel, 0.96 for the green channel, 0.99 for the red channel, 0.99 for the red-edge channel, and 0.99 for the NIR channel, indicating a very strong relationship between the measurements of spectroradiometer and the multispectral image.

The methodology employed involved the production of one bathymetric map based on field measurements and five multispectral images of varying dates and spatial resolutions. Figure 10 shows the coastal bathymetry of Coral Bay that was derived through the processing of the following data sets: (a) in situ SBES data collected on 3 December 2022; (b) PlanetScope image captured on 2 June 2022; (c) PlanetScope image captured on 6 December 2022; (d) PlanetScope image on 25 April 2023; (e) Sentinel 2 26 April 2023; and (f) DJIP4M images on 26 April 2023. Additionally, for each bathymetric map produced, a chart comparing the estimated and the in situ bathymetric data was created (Figure 11).

In order to assess the accuracy of the results, twenty percent of in situ data were used for the validation of the bathymetric information extracted from the satellite images and the DJIP4M data; the estimated RMSEs together with the correlation coefficient R^2 are shown in Table 3.

Table 3. R^2 and RMSE of the satellite and UAV derived bathymetry in relation to in situ measurements.

	Satellite	Date Acquisition	R^2	RMSE (m)
(a)	PlanetScope	2 June 2022	0.97	1.20
(b)	PlanetScope	6 December 2022	0.95	1.52
(c)	PlanetScope	25 April 2023	0.98	1.10
(d)	DJIP4M	26 April 2023	0.98	1.02
(e)	Sentinel 2	26 April 2023	0.98	0.92

The validation exercise resulted in RMSEs ranging from 0.92 to 1.52 m. The results for the PlanetScope bathymetry demonstrated a rather similar accuracy across the three sets. It is noted that only the December 2022 PlanetScope image was obtained on a date close to the collection of hydroacoustic information (03/12/22). The first PlanetScope image had been captured six months earlier, whereas the third PlanetScope image, the Sentinel 2 image and the DJIP4M data were acquired almost five months after the hydroacoustic survey. Nevertheless, the December 2022 PlanetScope bathymetry showed the lowest accuracy (RMSE 1.52 m), whilst the April bathymetry had the highest (RMSE 1.10 m). Interestingly, April Sentinel 2 and DJIP4M bathymetries, which were extracted from information obtained almost 5 months after the hydroacoustic survey, also showed low RMSEs and high correlation coefficients when compared with the bathymetry that was based on the in situ measurements. These discrepancies in accuracy were primarily attributed to the changing weather conditions.

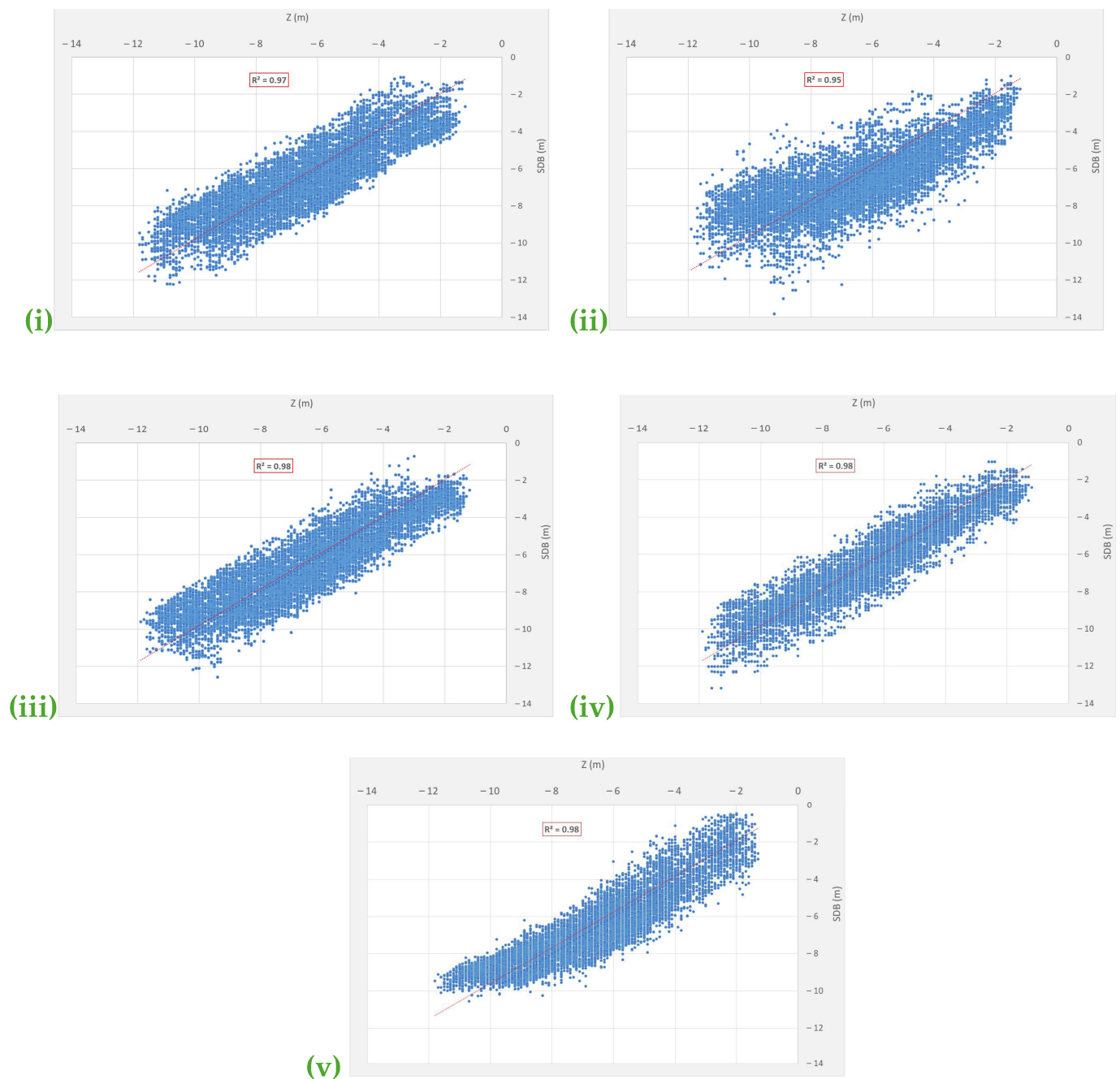


Figure 11. Comparison charts between the 20% of the in situ bathymetric data and estimated bathymetry with (i) PlanetScope on 2 June 2022, (ii) PlanetScope on 6 December 2022, (iii) PlanetScope on 25 April 2023, (iv) estimated bathymetry with Sentinel 2 on 2 June 2022 and (v) DJIP4M on 26 April 2023.

Additional processing was conducted to assess and mitigate geospatial errors in the bathymetric estimations. Given the variations in spatial resolution among the datasets, the derived bathymetry from the SBES measurements were individually resampled to match the resolution of each image. This approach ensured consistency in the comparison of bathymetric estimates across different sensors. Subsequently, error distribution maps were generated to illustrate the spatial variation in bathymetric accuracy as a function of the sensor type and acquisition date (Figure 12). These maps represent the error estimates corresponding to each bathymetric assessment outlined in Table 3 and provide a comprehensive evaluation of the accuracy of bathymetric estimations across different sensors and

acquisition dates. The maps show the error (in meters) between field measurements and estimated depths, with warmer colors (red) indicating higher errors and cooler colors (blue) representing lower errors. These maps reflect the error estimates for each bathymetric assessment.

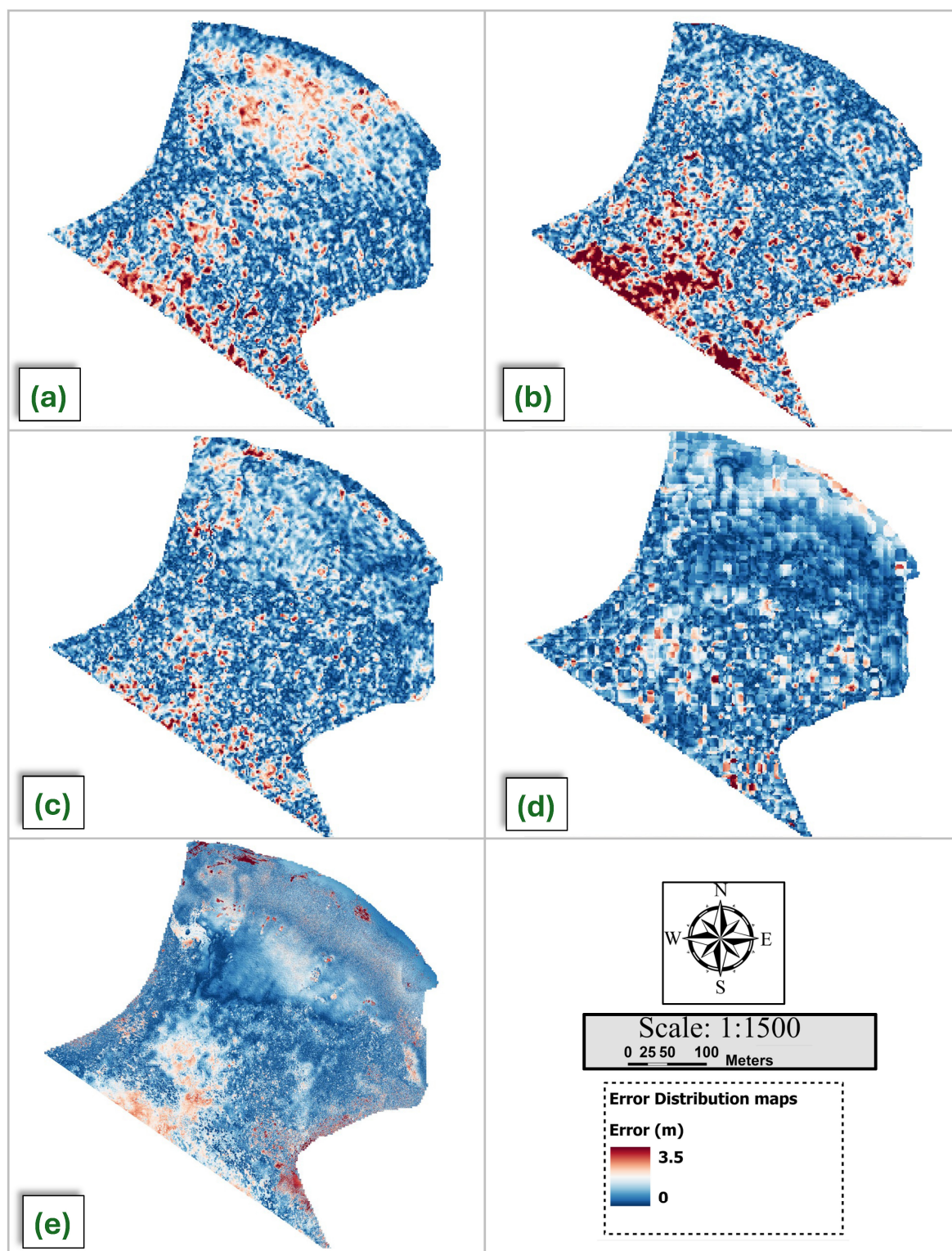


Figure 12. Error distribution maps of the in situ data and estimated bathymetry for (a) PlanetScope 2 June 2022; (b) PlanetScope 6 December 2022; (c) PlanetScope 25 April 2023; (d) Sentinel 2 26 April 2023; (e) DJIP4M 26 April 2023.

Analysis of the PlanetScope images (Figure 12a–c) revealed a generally heterogeneous distribution of errors across the study area. While some regions exhibited relatively low errors, signifying a strong correlation with field measurements, other areas, particularly near the boundaries of the mapping region and towards shallower waters, showed higher errors. Bathymetric estimates derived from DJIP4M imagery acquired on 26 April 2023 (Figure 12e) displayed lower errors than PlanetScope, with the map primarily featuring cooler colors. However, areas along the boundaries of the mapping region exhibited higher error levels. By contrast, the Sentinel-2 images, acquired on the same date (Figure 12d), demonstrated a more uniform spatial distribution of errors compared to those obtained from other sensors. The errors displayed in these images were generally lower across the study area, indicating a higher overall accuracy in bathymetric estimation when using this sensor.

Regarding morphology and habitat distribution, the high-resolution SSS images were interpreted and compared with the DJIP4M orthomosaic and the PlanetScope satellite image. Although the SSS analysis concerned the entire area covered by the marine survey (down to ~20 m depth, Figure 13), the correlation with the UAV and the satellite sensors was restricted to the limits of the embayment bounded by the two small capes (10–11 m depth, Figure 14), since it was obvious that they were not able to capture the deeper seafloor. The thorough SSS records and mosaic analysis allowed for seafloor classification in four reflectivity types (R) that represent specific substrate and habitat types. R4 was recorded only on sonographs deeper than 16 m; thus, it is only briefly described. The following reflectivity type spatial distribution estimations concern solely the common area imaged by all sensors.

R1 is associated with closely and irregularly spaced high- and low-reflectivity patches on a terrain of generally high to medium backscatter intensity, suggesting an uneven micro-relief corresponding to hard substrate (Figure 13). Camera footage also revealed an irregular and hard relief consisting of calcified bioaccumulations, but also the presence of small seagrass (*P. Oceanica*) patches developing within the hard substrate. Also, sediment pockets consisting of coarse sand and gravels and locally of small cobbles were occasionally distinguished in the camera images. Unfortunately, grab sampling attempts failed to retrieve sediment samples due to the hard nature of the seabed. The high reflectivity pattern of the hard substrate with its irregular micro-relief and the seagrass patches did not allow a reliable automatic classification and discrimination using the SonarWiz software v 8.0, but also a consistent manual (expert) interpretation and digitization. Thus, since R1 corresponds mainly to seabed with “hardgrounds” and coarse sediment and, to a minor extent, seagrass, all giving similar backscatter intensity, it was classified as “hard” substrate. R1 develops from about 11 to 6–7 m water depth, shows few randomly distributed targets in shallower waters and covers an area of 0.22 km², accounting for 66.4% of the c area commonly imaged by all sensors.

R2 displays a generally high backscatter intensity pattern and is characterized by rhythmic alterations of almost parallel high- and low-reflectivity stripes, implying the presence of a rippled seabed. R2 is distributed in the form of pockets of a varying extent and of irregular shape within R1, between ~11 and 6 m depth. The ripples are well formed, having a wavelength of 10–30 cm and a height of 4–10 cm. Their shape appears to be faintly asymmetrical, and their orientation is varying, as was also attested by the drop camera, probably suggesting a combined wave and current activity for their formation, abetted by the irregular micro-relief of the surrounding environment. Targeted sediment sampling from those pockets revealed coarse to very coarse sand both of biogenic and terrestrial origin with a mean grain size of -0.06 to 0.49ϕ . R2 occupies an area of 0.019 km² (5.6% of the commonly surveyed area).

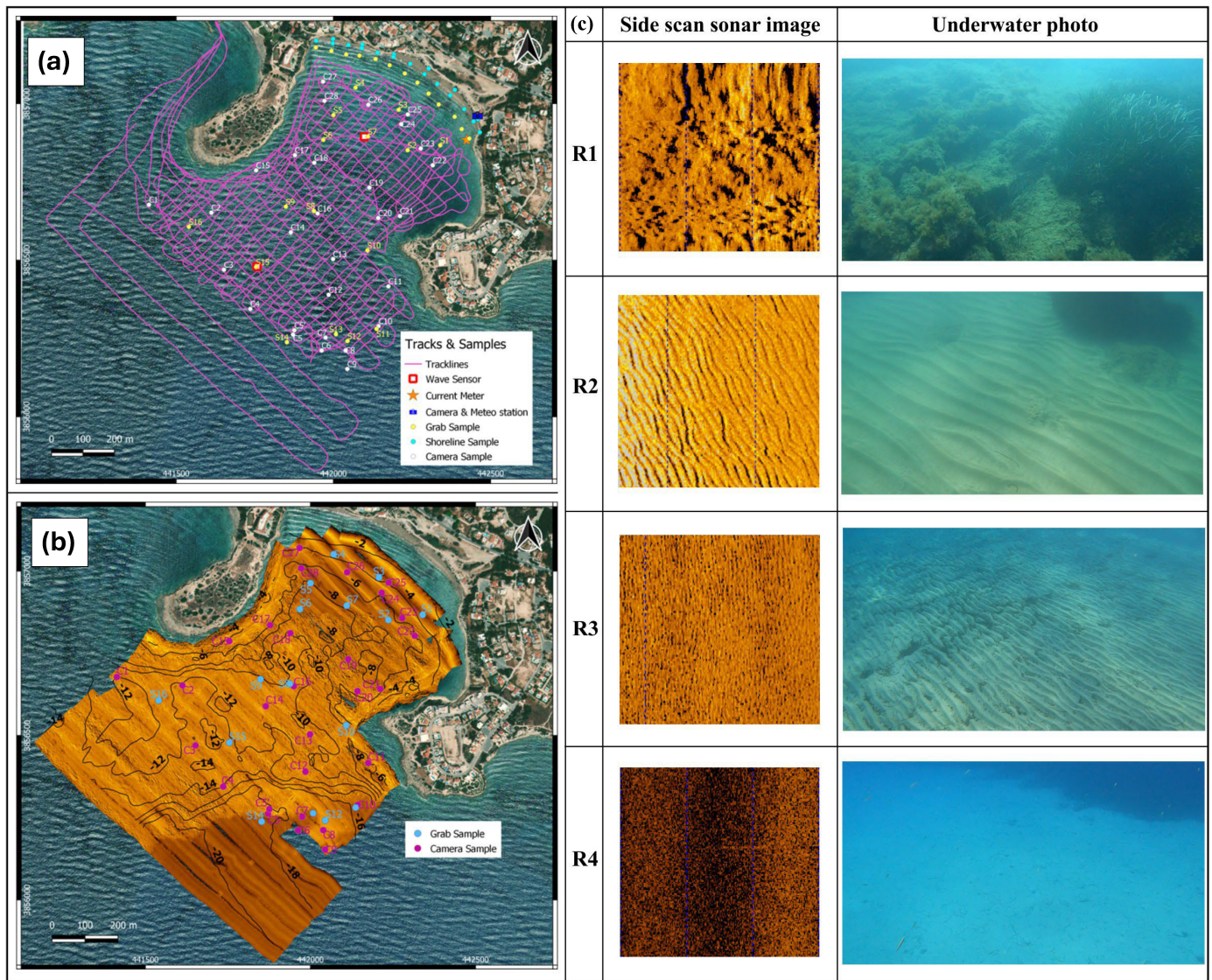


Figure 13. (a) Field data collection in the wider region, (b) SSS mosaic overlain by SBES bathymetry, grab samples and drop camera stations and (c) SSS reflectivity types (R1 to R4) with representative SSS images and underwater photos observed all over the study area.

R3 shows a medium backscatter intensity pattern developing over a smooth seabed. It was found to be shallower than 6–7 m and commonly includes areas or small pockets of ripples irregularly distributed. The ripples appear to be symmetrical, their orientation parallels the shoreline, and they have a wavelength and height of about 4–10 cm and 1–4 cm, respectively, being obviously smaller than those of R². They consist of medium to fine sand with a mean size of 1.89–2.99 Ø. R3 covers 0.09 km² (28% of the area surveyed by all three sensors).

Finally, the R4, which was recorded deeper than 16 m, is associated with low reflectivity and a featureless seabed, as was verified by drop camera images. Sediments over this area consist of very fine sand with a mean grain size of 3.00–3.14 Ø.

Orthomosaics generated using the DJIP4M data and PlanetScope imagery (resolution of 0.05 m and 3 m, respectively), acquired close to the date of the hydroacoustic data acquisition, were utilized to identify/demarcate seabed types/habitats and carry out comparisons with the in situ information. The analysis involved the classification of the orthomosaics utilizing the k-Nearest Neighbor (k-NN) algorithm for supervised classification. This process entails verification of data within sampled areas, thereby facilitating predictions of

the clustering of substrate types from the orthomosaic. Due to the small number of the SSS validation points by ground-truthing, additional control points were added to refine the orthomosaic's classification, based on the results of the SSS (Figure 14).

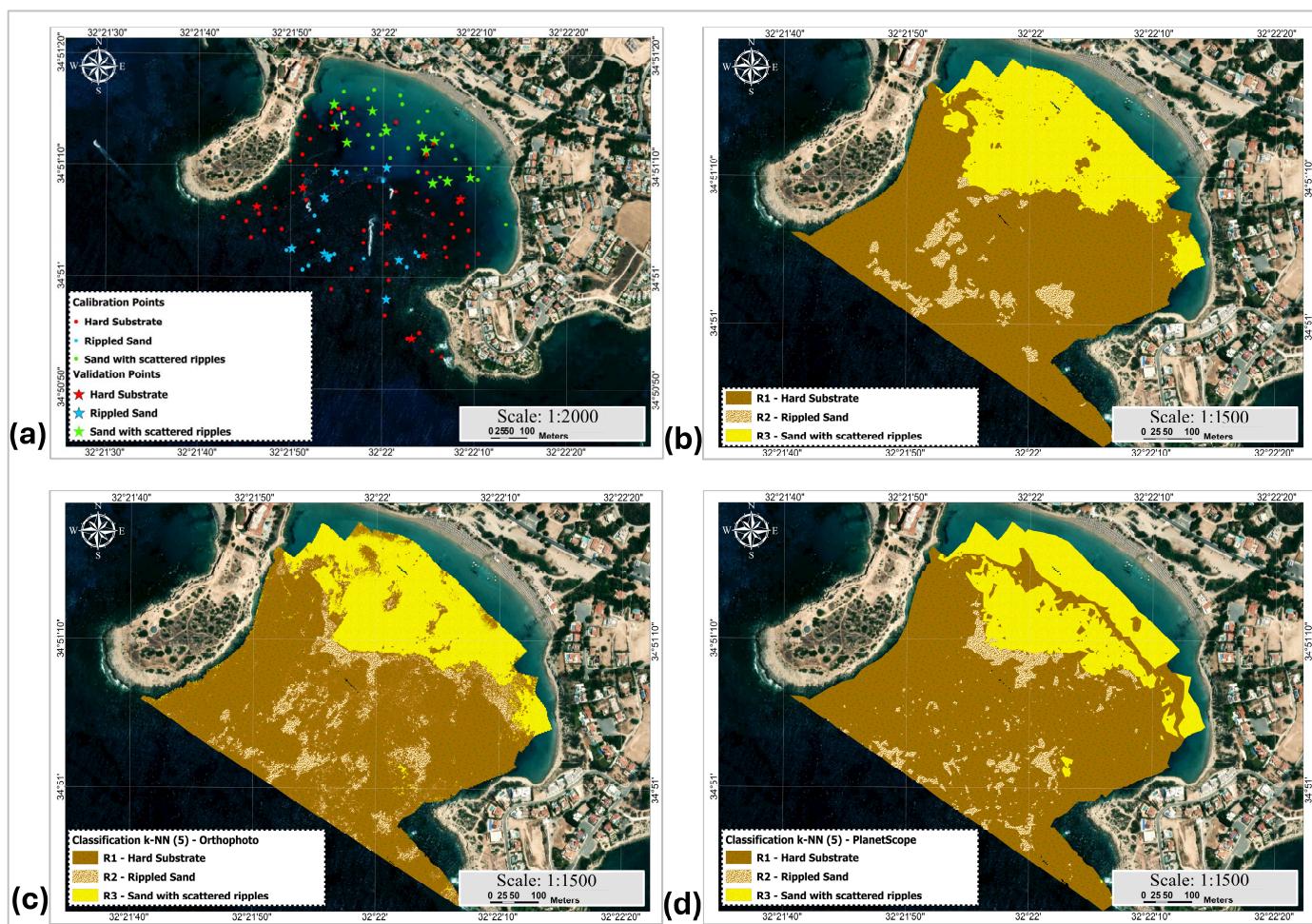


Figure 14. (a) Vector dataset containing 25 validation points (star shape) derived from camera dives and 100 calibration points created from the SSS mosaic (colored dots). Habitat maps from (b) SSS interpretation, (c) k-NN classification from the DJIP4M orthomosaic and (d) k-NN classification from the PlanetScope orthomosaic.

The comparison of the results of the SSS and the k-NN supervised classifications (Figure 14) showed some notable characteristics. According to the SSS interpretation, 66.4% of the seabed appraised by all three approaches is classified as “hard substrate” (R1), whereas according to the DJIP4M orthomosaic and the PlanetScope satellite image classifications, the hard substrate occupies 59% and 70% of the appraised area, respectively. It is obvious that there are discrepancies in the results of both orthomosaics in shallow waters since they indicate the presence of hard substrates (Figure 14) in areas where sands with scattered ripples (R3) were observed; this is particularly apparent in the satellite image classification.

In addition, the SSS classification indicates that 5.6% of the appraised area is associated with rippled sands (R2), whereas the classifications from the DJIP4M and the PlanetScope data indicate 15% and 7%, respectively. The larger discrepancy in the DJIP4M classification might be due to its high spatial resolution; while higher-resolution images may capture intricate details, they can also introduce higher variability and noise (e.g., sunglint, turbidity, waves) in the classification. Conversely, the lower-resolution satellite imagery yields more

consistent results compared to the SSS classification as it averages the spectra into larger pixels, effectively smoothing out local variations.

Finally, regarding the “Sand with scattered ripples” (R3) category, the SSS showed a spatial occurrence of 28%, the DJIP4M orthomosaic 26%, and the PlanetScope orthomosaic 23%. The discrepancies observed between the satellite imagery and the SSS results are mostly associated with the shallower areas of the bay.

A validation dataset comprising 1000 evaluation points was generated through a random spatial distribution to evaluate the accuracy of the orthomosaic classifications. This dataset was created by aligning the results obtained from the SSS with the corresponding reference values. Following this procedure, the values of the classified mosaics obtained from the DJIP4M and PlanetScope data were extracted into evaluation points, thereby facilitating the formulation of accuracy tables (Tables 4 and 5). These tables present comprehensive information on user accuracy, producer accuracy, overall accuracy and the Kappa index coefficient for all orthomosaic classifications.

Table 4. Accuracy matrix for the DJIP4M orthomosaic, using k-NN as the classifier (KIA: Kappa index of agreement).

		Ground Truth			
		Hard Substrate	Rippled Sand	Sand with Scattered Ripples	Sum
Training Data	Hard substrate	596	3	22	621
	Rippled sand	61	51	12	124
	Sand with scattered ripples	9	1	245	255
	Sum	666	55	279	1000
Producers’ accuracy		0.89	0.93	0.88	
Users’ accuracy		0.96	0.41	0.96	
KIA per class		0.88	0.44	0.91	
Total accuracy				0.89	
Overall, Kappa				0.79	

Table 5. Accuracy matrix for the PlanetScope satellite imagery, using k-NN as the classifier (KIA: Kappa index of agreement).

		Ground Truth			
		Hard Substrate	Rippled Sand	Sand with Scattered Ripples	Sum
Training Data	Hard substrate	596	37	56	689
	Rippled sand	49	17	9	75
	Sand with scattered ripples	21	1	214	236
	Sum	666	55	279	1000
Producers’ accuracy		0.89	0.31	0.77	
Users’ accuracy		0.87	0.23	0.91	
KIA per class		0.94	0.73	0.84	
Total accuracy				0.83	
Overall, Kappa				0.63	

The classification results obtained from the DJIP4M orthomosaic (Table 4) estimate a high overall accuracy of 0.89 and a Kappa coefficient of 0.79, indicating a good agreement

between the predicted classifications and the reference ground truthing. A significant issue that arose was the misclassification of the categories “sand with scattered ripples” and “hard substrate”. The findings revealed that in 22 instances, “sand with scattered ripples” was mistakenly classified as “hard substrate”, while in nine cases, “hard substrate” was inaccurately identified as “sand with scattered ripples”.

The “rippled sand” category also displayed some confusion with both “hard substrate” and “sand with scattered ripples”. Out of 124 reference samples for “rippled sand”, 61 were incorrectly labeled as “hard substrate”. This shows that the small differences between these two categories are difficult to be identified with k-NN. Moreover, the “rippled sand” category had a low user accuracy of 0.41, indicating a high number of false positives in its classification. The Kappa index of 0.44 for this class further emphasizes the challenge in accurately identifying “rippled sand” from other substrates.

By contrast, “sand with scattered ripples” was classified accurately. Out of 279 cases, 245 were correctly identified, giving a producer accuracy of 0.88 and a user accuracy of 0.96. While the classifier performed well with this category, a small number of “sand with scattered ripples” samples were still misclassified, especially as “hard substrate”. The Kappa index of 0.91 for this category confirms its strong classification performance.

Overall, the “hard substrate” category achieved the highest producer’s accuracy at 0.89, signifying the model’s strong performance for this class. In comparison, the “rippled sand” category exhibited the lowest producer’s accuracy, highlighting the model’s difficulties in effectively classifying this seabed type. User accuracy was found to be highest for the “sand with scattered ripples” category at 0.96, indicating a high skill in predicting this class. Conversely, the “rippled sand” category displayed the lowest user accuracy, registering only 0.41, indicating large classification challenges for this seabed type, possibly due to potential spectral similarities or other environmental complexities.

The results derived from the PlanetScope classification (Table 5) also identified the “hard substrate” as the category with the highest producer’s accuracy (0.89), corroborating the UAV orthomosaic findings. A key observation was the confusion in classifying “rippled sand”, which has a low producer’s accuracy of 0.31. This indicates that many actual “rippled sand” samples were misclassified. The user’s accuracy of 0.23 shows that many pixels labeled as “rippled sand” belong to other types, mainly hard substrate (49 cases) and “sand with scattered ripples” (9 cases). The Kappa Index of Agreement (KIA) is also low at 0.73, suggesting that the k-NN classifier struggles to differentiate “rippled sand” using the PlanetScope imagery.

On the other hand, “hard substrate” has a high classification accuracy, correctly identifying 596 out of 666 instances, resulting in a producer’s accuracy of 0.89 and a user’s accuracy of 0.87. However, 37 samples of “rippled sand” were misclassified as “hard substrate”, indicating some overlap in spectral reflectance. Additionally, 56 pixels of “sand with scattered ripples” were wrongly classified as “hard substrate”.

Despite having the highest number of correct classifications (214 out of 279), “sand with scattered ripples” also faced misclassifications, mainly with the “hard substrate” (21 cases). Although it managed to achieve a high user’s accuracy of 0.91, the lower value of the producer’s accuracy (0.77) indicates that some actual samples were misclassified into other categories, particularly “hard substrate”.

Overall, the “rippled sand” category showed a significantly lower producer’s accuracy (0.31), further emphasizing the persistent difficulty across datasets to distinguish this sediment type. The highest user accuracy in the PlanetScope orthomosaic classification was found for “sand with scattered ripples” at 0.91, while “rippled sand” had the lowest user accuracy at 0.23. The Kappa coefficient for this classification was 0.63, indicating a moderate agreement between the classification outputs and the reference data, which is

notably lower compared with the coefficient achieved with the DJIP4M dataset. These discrepancies suggest that differences in spatial resolution and spectral characteristics between UAV and satellite imagery can influence the accuracy and reliability of seabed classification.

5. Discussion

Coastal mapping efforts have increased rapidly in recent decades aiming to collect geo-spatial data of high resolution and precision in order to credibly inform models/tools to support sustainable coastal development, to manage different anthropogenic and climatic threats to the coastal human and natural environments and assist conservation goals. The majority of such information is now provided by Earth Observation (EO) technologies, which have been influenced by scientific innovations in all fields of remote sensing (satellite, aerial, marine) and progress in geospatial data analysis [21,31,34,39,92]. Yet, although the coastal environment attracts interdisciplinary research, which commonly utilizes similar survey techniques, there have been few efforts to integrate/inter-validate them for use in both the onshore and inshore coastal areas.

The approaches and tools used in such studies depend on the spatial scale/scope of the application [93]. For large-scale applications, satellite imagery appears to be an indispensable tool, as it can provide consistent, although intermittent, observations of the shoreline variability and seabed bathymetry and habitats [94], especially when the data availability from a wide range of EO platforms and sensors is considered. However, the spatial resolution and the fact that satellite observations are dependent on the environmental conditions present at the time of their acquisition create several challenges, particularly in small-scale studies that require information of high resolution and accuracy. Thus, a major issue emerges when considering the dynamic nature of the wider coastal environment and its short-term variability, which is very difficult to monitor, since remote sensing techniques offer only instant time snapshots without being able to offer a continuous picture of the coastal terrain over time [38]. Therefore, beach modifications in the intervening periods are not captured, and frequent changes occurring along the coastal areas cannot easily/safely be interpreted, leading to misleading interpretations of the prevailing processes. Beach optical monitoring systems may serve the needs of continuous detection in high precision topography and shoreline changes, but only along spatially restricted stretches of beaches [94,95]. On the other hand, only repeated aerial and marine sensing surveys, either seasonal or before and after storm events (when considering morphodynamic monitoring), can produce comparable but timely intermittent and costly mapping products.

In the present study, a “holistic” approach was employed. Information from a wide range of remote sensing approaches/tools were utilized to produce high resolution/accuracy maps of both the onshore and inshore parts of Coral Bay. A comparison of DEMs generated using a series of observations from satellite and UAV-mounted sensors, over an almost one-year period, provided clear evidence of beach modifications (i.e., shoreline and elevation changes), highlighting the dynamic nature of coastal processes. Significant beach elevation changes were observed during the more energetic winter–early spring period; nevertheless, there has been also evidence of a tendency for beach recovery during the time of observations. The repeated topographic observations also suggested alongshore variability in the patterns of beach accretion and erosion, which corroborated previous studies in the area [38], with beach accretion occurring mostly along the south-eastern stretch of the beach and erosion along the northwestern part. These varying beach dynamics emphasize the need for detailed hydrodynamic and morphodynamic modeling, which should be set up (and forced) on the basis of geomorphological information of high resolution and accuracy [38,59]. These results also align with previous research empha-

sizing the utility of UAV-based monitoring for detecting and quantifying morphological changes [75,96].

Repeated TLS surveys along a small part of the sea cliff of the southern promontory bounding Coral Bay revealed a substantial degree of spatiotemporal variability due to erosional processes. They captured fine-scale geomorphological changes, enabling a comprehensive understanding of the cliff dynamics over time. Instabilities were detected to affect the middle to lower part of the central and easternmost part of the sea cliff posing a threat to residential properties at the top of the cliff. Despite the technical measures that have been implemented to mitigate wave-driven erosion, the sea cliff still appears to be under erosion, which might be attributed to other environmental forcing factors, such as pluvial erosion of the loosely consolidated sediments and regional seismic activity [44,97]. These findings are in line with prior studies demonstrating the potential for TLS-based point cloud comparisons to effectively detect fine-scale cliff morphodynamics [44,98,99].

In addition to monitoring the onshore morphology using remote sensing techniques, the study incorporated bathymetric and marine habitat mapping of the inshore area in order to assess the beach dynamic processes in a 'holistic', integrated manner. Previous research has demonstrated the efficacy of remote sensing techniques, albeit with several constraints due to various environmental factors [35,100]. These constraints can result in considerable inaccuracies in both bathymetric estimates and the classification of marine habitats. The primary source of error is often related to weather conditions. The presence of suspended fine sediments on the seabed and seasonal turbidity, which is influenced by hydrodynamic conditions, further compromises the accuracy of depth estimations [37,101]. Moreover, atmospheric corrections applied to the satellite images, which serve as the main data source, can introduce additional errors. Accurate atmospheric corrections are essential, as any inaccuracies in this process can significantly affect the reliability of the bathymetric results [102].

Specifically, sunlight reflection had the most pronounced effect, particularly in high-resolution imagery. In shallow water areas, increased surface reflection introduced significant noise, leading to considerable errors in both depth measurements retrieval and benthic classification. Furthermore, turbidity, especially during the winter months, negatively impacted the accuracy of remote sensing results. This effect is likely attributed to reduced water clarity, which prevents the penetration of spectral signals and increases uncertainty in depth estimation and substrate classification.

In this study, the bathymetric assessment was carried out using satellite and UAV mounted sensors together with hydroacoustics. This exercise showed relatively good results, with the estimated RMSEs in three different surveys ranging between 0.92 and 1.52 m. PlanetScope satellite data yielded the best results in April 2023 (RMSE of 1.10 m). Despite the high precision and abundant SBES data collection in December 2022, the accuracy of estimations in April and June surpassed Decembers' results by 27% and 21%, respectively, likely due to more favorable meteorological conditions during these periods, as also noted in related studies [103,104]. Interestingly, the spatial resolution analysis revealed that the lowest resolution dataset, derived from Sentinel 2 imagery, yielded the most accurate results (RMSE of 0.92 m). This finding is noteworthy, as it contrasts with the typical expectation that higher-resolution data collected the same day with the UAV would produce more precise bathymetric estimations [37,105,106]. However, significant deviations were noted in the shallow areas of the bay (0–1.8 m), where accuracy was compromised due to the limited collection of field data. In these areas, GNSS-measured points were used instead of SBES data, since very shallow depths limit safe surveying operations and bathymetric measurements. Yet, considering the dynamic nature of the inshore environment, high-resolution images may be affected by suspended particles

and water column perturbations, leading to increased errors in depth estimation [37,107]. Therefore, while higher-resolution images provide enhanced spatial detail, they can also introduce noise and variability. Consequently, lower-resolution images can be more reliable for broad-scale bathymetric mapping in specific conditions. Comparative analysis of multispectral UAV data and PlanetScope satellite information showed that the UAV data achieved higher accuracy, outperforming the satellite data by at least 7% due to its higher spatial resolution.

The classification and mapping of the seabed habitats/types were precisely performed using high-resolution side scan sonar sonographs, ground-truthed by drop camera images and sediment sampling. The results were used both for calibration and validation of the high spatial resolution data obtained by the UAV and satellite sensors [108,109]. The analysis revealed three habitat types (hard substrate, rippled sand, sand with scattered ripples) and their distribution in the commonly studied area by all remote sensing techniques. Comparison of the different sensor datasets revealed a strong correlation between the UAV data and field (hydroacoustic) measurements, facilitating habitat mapping with remarkable precision and achieving a total accuracy of 89%. In comparison, satellite imagery, although of lower resolution, also yielded good results (total accuracy of 83%). Even though these results are promising, it is crucial to consider alternative classification methods, as various techniques may yield different levels of accuracy influenced by factors such as image resolution and the complexity of marine substrates. Utilizing a range of classification approaches, such as Maximum Likelihood Classification (MLC), Random Forest (RF), and Artificial Neural Networks (ANN), the overall classification performance is expected to have a better potential to enhance. The superior performance of the high-resolution UAV data highlights its effectiveness in capturing habitat details, while the very satisfactory performance of the satellite imagery demonstrated its potential for seabed classification at smaller spatial scales, particularly in scenarios where high-resolution data may not be readily available. However, the use of a single UAV multispectral image, due to the data collection constraints, represents a limitation of this study. The absence of additional high-resolution imagery restricts the ability to capture temporal variability in water conditions and spectral responses, which may influence the accuracy of both bathymetric estimations and habitat classification. Although the available imagery was acquired under optimal environmental conditions to minimize external influences, the integration of multitemporal UAV data in future research would enhance the temporal robustness of the analyses. This approach would allow for more comprehensive assessments of environmental variability, the consistency of spatial resolution outputs, and the overall performance of the models.

6. Conclusions

This study focused on developing a multi-integrative remote sensing approach involving satellite, aerial, terrestrial, and underwater methods to create a holistic model of coastal geomorphology and habitats in one of the most valuable coastal environments of Cyprus, Coral Bay. The integration of high-spatial-resolution information from marine (side scan sonar), aerial (UAV) and satellite sensors proved to have built a strong data framework for analyzing the coastal terrain. Overall, the workflow adopted in this study provides a robust approach for multilevel monitoring of coastal geomorphology and marine habitat mapping, leveraging the power of multiple remote sensing techniques and advanced data processing methods. The results are considered highly promising, demonstrating the potential of remote sensing for dealing with dynamic coastal environments. The findings of this study also designate the utility of exploiting data from various types of sensors, sometimes of lower resolution, that can combine effectively to yield the coastal landscape.

Yet, future advancements, such as the integration of hyperspectral imaging, LiDAR-equipped UAVs, and next-generation sonar systems, are expected to refine depth estimations and habitat classification, effectively addressing existing limitations in spatial resolution and data reliability. Moreover, the automation of data processing and the adoption of artificial intelligence-driven algorithms can potentially increase classification precision. Expanding temporal monitoring to include multi-temporal and real-time observations can significantly strengthen coastal and marine assessments, fostering more adaptive and data-driven environmental management strategies.

Author Contributions: Conceptualization, T.H., E.E. and C.M.; methodology, T.H., E.E. and C.M.; software, E.E., A.C., I.T.P., O.P.A., I.N.M. and D.C.; validation, E.E., I.N.M., A.C., I.T.P., O.P.A. and D.C.; formal analysis, E.E. and C.M.; investigation, T.H., E.E. and C.M.; resources, T.H., E.E., I.N.M., A.C., I.T.P., O.P.A., C.M., D.C., A.V., J.K.; data curation, T.H., E.E., A.C., I.T.P., O.P.A. and C.M.; writing—original draft preparation, E.E.; writing—review and editing, T.H., C.M., N.S., A.V. and D.H.; visualization, E.E.; supervision, T.H., A.V. and D.H. All authors have read and agreed to the published version of the manuscript.

Funding: This research was supported by the research project Coastal erosion due to climate change: assessment and ways of effective response in tourist areas of the North Aegean and Cyprus with acronym «BEACHTECH», co-funded by the European Regional Development Fund (ERDF) and national funds of Greece and Cyprus under the Cooperation Program “INTERREG V-A Greece-Cyprus 2014–2020”.

Data Availability Statement: The authors declare no conflicts of interest.

Acknowledgments: The authors would like to acknowledge the support of the ‘ERATOSTHENES: Excellence Research Centre for Earth Surveillance and SpaceBased Monitoring of the Environment-‘EXCELSIOR’ project (<https://excelsior2020.eu/>, accessed on 11 October 2021) that has received funding from the European Union’s Horizon 2020 research and innovation programme under grant agreement No 857510 (Call: WIDESPREAD-01-2018-2019 Teaming Phase 2) and the Government of the Republic of Cyprus through the Directorate General for European Programmes, Coordination and Development.

Conflicts of Interest: The authors declare no conflicts of interest.

References

1. Field, C.B.; Barros, V.; Stocker, T.F.; Qin, D.; Dokken, D.J.; Ebi, K.J.; Plattner, G.K.; Allen, S.K.; Tignor, M.; Midgley, P.M. *Managing the Risks of Extreme Events and Disasters to Advance Climate Change Adaptation: A Special Report of Working Groups I and II of the Intergovernmental Panel on Climate Change*; Cambridge University Press: Cambridge, UK; New York, NY, USA, 2012; 582p. [\[CrossRef\]](#)
2. Roy, P.; Pal, S.C.; Chakraborty, R.; Chowdhuri, I.; Saha, A.; Shit, M. Effects of Climate Change and Sea-Level Rise on Coastal Habitat: Vulnerability Assessment, Adaptation Strategies and Policy Recommendations. *J. Environ. Manag.* **2023**, *330*, 117187. [\[CrossRef\]](#) [\[PubMed\]](#)
3. Neumann, B.; Vafeidis, A.T.; Zimmermann, J.; Nicholls, R.J. Future Coastal Population Growth and Exposure to Sea-Level Rise and Coastal Flooding—A Global Assessment. *PLoS ONE* **2015**, *10*, e0118571. [\[CrossRef\]](#) [\[PubMed\]](#)
4. Ackerman, R. *The Nest Environment and the Embryonic Development of Sea Turtles*; Lutz, P.L., Musick, J.A., Eds.; CRC Press: Boca Raton, FL, USA, 2017; Volume 1, ISBN 9780203737088.
5. Orlando, L.; Ortega, L.; Defeo, O. Perspectives for Sandy Beach Management in the Anthropocene: Satellite Information, Tourism Seasonality, and Expert Recommendations. *Estuar. Coast. Shelf Sci.* **2021**, *262*, 107597. [\[CrossRef\]](#)
6. Bozzeda, F.; Ortega, L.; Costa, L.L.; Fanini, L.; Barboza, C.A.M.; McLachlan, A.; Defeo, O. Global Patterns in Sandy Beach Erosion: Unraveling the Roles of Anthropogenic, Climatic and Morphodynamic Factors. *Front. Mar. Sci.* **2023**, *10*, 1270490. [\[CrossRef\]](#)
7. Landry, C.E.; Turner, D.; Allen, T. Hedonic Property Prices and Coastal Beach Width. *Appl. Econ. Perspect. Policy* **2022**, *44*, 1373–1392. [\[CrossRef\]](#)
8. UNWTO *International Tourism Highlights*, 2024 ed.; World Tourism Organization: Madrid, Spain, 2024; ISBN 978-92-844-2579-2.

9. Guisado-Pintado, E.; Jackson, D.W.T. Coastal Impact From High-Energy Events and the Importance of Concurrent Forcing Parameters: The Cases of Storm Ophelia (2017) and Storm Hector (2018) in NW Ireland. *Front. Earth Sci.* **2019**, *7*, 454617. [\[CrossRef\]](#)
10. Vousdoukas, M.I.; Ranasinghe, R.; Mentaschi, L.; Plomaritis, T.A.; Athanasiou, P.; Luijendijk, A.; Feyen, L. Sandy Coastlines under Threat of Erosion. *Nat. Clim. Change* **2020**, *10*, 260–263. [\[CrossRef\]](#)
11. Almar, R.; Ranasinghe, R.; Bergsma, E.W.J.; Diaz, H.; Melet, A.; Papa, F.; Vousdoukas, M.; Athanasiou, P.; Dada, O.; Almeida, L.P.; et al. A Global Analysis of Extreme Coastal Water Levels with Implications for Potential Coastal Overtopping. *Nat. Commun.* **2021**, *12*, 3775. [\[CrossRef\]](#) [\[PubMed\]](#)
12. Monioudi, I.N.; Velegrakis, A.F. Beach Carrying Capacity at Touristic 3S Destinations: Its Significance, Projected Decreases and Adaptation Options under Climate Change. *J. Tour. Hosp.* **2022**, *11*, 500. [\[CrossRef\]](#)
13. Komar, P.D. *Beach Processes and Sedimentation*, 2nd ed.; Prentice Hall: Englewood Cliffs, NJ, USA, 1998; ISBN 0137549385, 9780137549382.
14. Siemens, T.; Bastola, S. Depth of Closure, a Review of Empirical Formulae and Assessment of Climate Change along the Coast of Louisiana. *J. Coast. Conserv.* **2024**, *28*, 71. [\[CrossRef\]](#)
15. Tsuguo, S. Sunamura Tsuguo Processes of Sea Cliff and Platform Erosion. In *CRC Handbook of Coastal Processes and Erosion*; CRC Press: Boca Raton, FL, USA, 2018; pp. 233–266, ISBN 9781351072908.
16. Earlie, C.; Masselink, G.; Russell, P. The Role of Beach Morphology on Coastal Cliff Erosion under Extreme Waves. *Earth Surf. Process. Landf.* **2018**, *43*, 1213–1228. [\[CrossRef\]](#)
17. Serrano, E.; de Sanjosé, J.J.; Gómez-Lende, M.; Sánchez-Fernández, M.; Gómez-Gutiérrez, A. Coastal Retreat and Sea-Cliff Dynamic on the North Atlantic Coast (Gerra Beach, Cantabrian Coast, Spain). *Environ. Earth Sci.* **2024**, *83*, 89. [\[CrossRef\]](#)
18. Allenbach, K.; Garonna, I.; Herold, C.; Monioudi, I.; Giuliani, G.; Lehmann, A.; Velegrakis, A.F. Black Sea Beaches Vulnerability to Sea Level Rise. *Environ. Sci. Policy* **2015**, *46*, 95–109. [\[CrossRef\]](#)
19. Monioudi, I.N.; Velegrakis, A.F.; Chatzistratis, D.; Vousdoukas, M.I.; Savva, C.; Wang, D.; Bove, G.; Mentaschi, L.; Paprotny, D.; Morales-Nápoles, O.; et al. Climate Change—Induced Hazards on Touristic Island Beaches: Cyprus, Eastern Mediterranean. *Front. Mar. Sci.* **2023**, *10*, 1188896. [\[CrossRef\]](#)
20. Monioudi, I.N.; Velegrakis, A.F.; Chatzipavlis, A.E.; Rigos, A.; Karambas, T.; Vousdoukas, M.I.; Hasiotis, T.; Koukourouli, N.; Peduzzi, P.; Manoutsoglou, E.; et al. Assessment of Island Beach Erosion Due to Sea Level Rise: The Case of the Aegean Archipelago (Eastern Mediterranean). *Nat. Hazards Earth Syst. Sci.* **2017**, *17*, 449–466. [\[CrossRef\]](#)
21. Misiuk, B.; Brown, C.J. Benthic Habitat Mapping: A Review of Three Decades of Mapping Biological Patterns on the Seafloor. *Estuar. Coast. Shelf Sci.* **2024**, *296*, 108599. [\[CrossRef\]](#)
22. Manes, S.; Gama-Maia, D.; Vaz, S.; Pires, A.P.; Tardin, R.H.; Maricato, G.; Bezerra, D.d.S.; Vale, M.M. Nature as a Solution for Shoreline Protection against Coastal Risks Associated with Ongoing Sea-Level Rise. *Ocean Coast. Manag.* **2023**, *235*, 106487. [\[CrossRef\]](#)
23. Nourdi, N.F.; Raphael, O.; Achab, M.; Loudi, Y.; Rudant, J.P.; Minette, T.E.; Kambia, P.; Claude, N.J.; Romaric, N. Integrated Assessment of Coastal Vulnerability in the Bonny Bay: A Combination of Traditional Methods (Simple and AHP) and Machine Learning Approach. *Estuaries Coasts* **2024**, *47*, 2670–2695. [\[CrossRef\]](#)
24. Andreadis, O.; Chatzipavlis, A.; Hasiotis, T.; Monioudi, I.; Manoutsoglou, E.; Velegrakis, A. Assessment of and Adaptation to Beach Erosion in Islands: An Integrated Approach. *J. Mar. Sci. Eng.* **2021**, *9*, 859. [\[CrossRef\]](#)
25. Deng, J.; Yu, H. Modelling Coastal Morphodynamic Evolution under Human Impacts: A Review. *J. Mar. Sci. Eng.* **2023**, *11*, 1426. [\[CrossRef\]](#)
26. Karambas, T.V.; Samaras, A.G. An Integrated Numerical Model for the Design of Coastal Protection Structures. *J. Mar. Sci. Eng.* **2017**, *5*, 50. [\[CrossRef\]](#)
27. Gallerano, F.; Cannata, G.; Lasaponara, F. A New Numerical Model for Simulations of Wave Transformation, Breaking and Long-Shore Currents in Complex Coastal Regions. *Int. J. Numer. Methods Fluids* **2016**, *80*, 571–613. [\[CrossRef\]](#)
28. Ranasinghe, R. Assessing Climate Change Impacts on Open Sandy Coasts: A Review. *Earth-Sci. Rev.* **2016**, *160*, 320–332. [\[CrossRef\]](#)
29. Peduzzi, P.; Velegrakis, A.; Chatenoux, B.; Estrella, M.; Karambas, T. Assessment of the Role of Nearshore Marine Ecosystems to Mitigate Beach Erosion: The Case of Negril (Jamaica). *Environments* **2022**, *9*, 62. [\[CrossRef\]](#)
30. Velegrakis, A.F.; Trygonis, V.; Chatzipavlis, A.E.; Karambas, T.; Vousdoukas, M.I.; Ghionis, G.; Monioudi, I.N.; Hasiotis, T.; Andreadis, O.; Psarros, F. Shoreline Variability of an Urban Beach Fronted by a Beachrock Reef from Video Imagery. *Nat. Hazards* **2016**, *83*, 201–222. [\[CrossRef\]](#)
31. Velegrakis, A.F.; Chatzistratis, D.; Chalazas, T.; Armaroli, C.; Schiavon, E.; Alves, B.; Grigoriadis, D.; Hasiotis, T.; Ieronymidi, E. Earth Observation Technologies, Policies and Legislation for the Coastal Flood Risk Assessment and Management: A European Perspective. *Anthr. Coasts* **2024**, *7*, 3. [\[CrossRef\]](#)

32. Pardo-Pascual, J.E.; Almonacid-Caballer, J.; Cabezas-Rabadán, C.; Fernández-Sarría, A.; Armaroli, C.; Ciavola, P.; Montes, J.; Souto-Ceccon, P.E.; Palomar-Vázquez, J. Assessment of Satellite-Derived Shorelines Automatically Extracted from Sentinel-2 Imagery Using SAET. *Coast. Eng.* **2024**, *188*, 104426. [\[CrossRef\]](#)
33. Palomar-Vázquez, J.; Pardo-Pascual, J.E.; Almonacid-Caballer, J.; Cabezas-Rabadán, C. Shoreline Analysis and Extraction Tool (SAET): A New Tool for the Automatic Extraction of Satellite-Derived Shorelines with Subpixel Accuracy. *Remote Sens.* **2023**, *15*, 3198. [\[CrossRef\]](#)
34. Capperucci, R.M.; Kubicki, A.; Holler, P.; Bartholomä, A. Sidescan Sonar Meets Airborne and Satellite Remote Sensing: Challenges of a Multi-Device Seafloor Classification in Extreme Shallow Water Intertidal Environments. *Geo-Mar. Lett.* **2020**, *40*, 117–133. [\[CrossRef\]](#)
35. He, J.; Zhang, S.; Cui, X.; Feng, W. Remote Sensing for Shallow Bathymetry: A Systematic Review. *Earth-Sci. Rev.* **2024**, *258*, 104957. [\[CrossRef\]](#)
36. Viaña-Borja, S.P.; González-Villanueva, R.; Alejo, I.; Stumpf, R.P.; Navarro, G.; Caballero, I. Satellite-Derived Bathymetry Using Sentinel-2 in Mesotidal Coasts. *Coast. Eng.* **2025**, *195*, 104644. [\[CrossRef\]](#)
37. Evagorou, E.; Argyriou, A.; Papadopoulos, N.; Mettas, C.; Alexandrakakis, G.; Hadjimitsis, D. Evaluation of Satellite-Derived Bathymetry from High and Medium-Resolution Sensors Using Empirical Methods. *Remote Sens.* **2022**, *14*, 772. [\[CrossRef\]](#)
38. Hasiotis, T.; Andreadis, O.; Chatzipavlis, A.; Mettas, C.; Evagorou, E.; Kountouri, J.; Hadjimitsis, D.; Christofi, D.; Loizidou, M.; Chrysostomou, G. A Holistic High-Resolution Monitoring Approach in Studying Coastal Erosion of a Highly Touristic Beach, Coral Bay, Cyprus. In Proceedings of the Ninth International Conference on Remote Sensing and Geoinformation of the Environment (RSCy2023), Ayia Napa, Cyprus, 3–5 April 2023; Volume 12786, pp. 376–385. [\[CrossRef\]](#)
39. Valdazo, J.; Ferrer, N.; Vega, C.; Martín, J.; Luque, Á.; Bergasa, O. Mapping Marine Habitats in a Shallow Beach-Reef Environment Combining Direct Methods and Hyperspectral Remote Sensing. *Ocean Coast. Manag.* **2024**, *255*, 107231. [\[CrossRef\]](#)
40. Specht, M. Methodology for Performing Bathymetric and Photogrammetric Measurements Using UAV and USV Vehicles in the Coastal Zone. *Remote Sens.* **2024**, *16*, 3328. [\[CrossRef\]](#)
41. Tiškus, E.; Vaičiūtė, D.; Bučas, M.; Gintauskas, J. Evaluation of Common Reed (*Phragmites australis*) Bed Changes in the Context of Management Using Earth Observation and Automatic Threshold. *Eur. J. Remote Sens.* **2023**, *56*, 100–114. [\[CrossRef\]](#)
42. Bio, A.; Gonçalves, J.A.; Magalhães, A.; Pinheiro, J.; Bastos, L. Combining Low-Cost Sonar and High-Precision Global Navigation Satellite System for Shallow Water Bathymetry. *Estuaries Coasts* **2022**, *45*, 1000–1011. [\[CrossRef\]](#)
43. Guillén, J.; Simarro, G.; Calvete, D.; Ribas, F.; Fernández-Mora, A.; Orfila, A.; Falqués, A.; de Swart, R.; Sancho-García, A.; Durán, R. Sediment Leakage on the Beach and Upper Shoreface Due to Extreme Storms. *Mar. Geol.* **2024**, *468*, 107207. [\[CrossRef\]](#)
44. Panagou, T.; Hasiotis, T.; Velegrakis, A.; Karambas, T.; Oikonomou, E.; Dimitriadis, C. Erosion Status of a Sea Cliff Promontory Bounding an Ecologically Important Beach. *J. Coast. Conserv.* **2020**, *24*, 1–17. [\[CrossRef\]](#)
45. Andriolo, U.; Almeida, L.P.; Almar, R. Coupling Terrestrial LiDAR and Video Imagery to Perform 3D Intertidal Beach Topography. *Coast. Eng.* **2018**, *140*, 232–239. [\[CrossRef\]](#)
46. Brodie, K.L.; Slocum, R.K.; McNinch, J.E. New Insights into the Physical Drivers of Wave Runup from a Continuously Operating Terrestrial Laser Scanner. In Proceedings of the Ocean, 2012 MTS/IEEE Harnessing Power Ocean, Hampton Roads, VA, USA, 14–19 October 2012. [\[CrossRef\]](#)
47. Harry, M.; Zhang, H.; Lemckert, C.; Colleter, G.; Blenkinsopp, C. Observation of Surf Zone Wave Transformation Using LiDAR. *Appl. Ocean Res.* **2018**, *78*, 88–98. [\[CrossRef\]](#)
48. Klopfer, F.; Hämmerle, M.; Höfle, B. Assessing the Potential of a Low-Cost 3-D Sensor in Shallow-Water Bathymetry. *IEEE Geosci. Remote Sens. Lett.* **2017**, *14*, 1388–1392. [\[CrossRef\]](#)
49. Panagou, T.; Oikonomou, E.; Hasiotis, T.; Velegrakis, A.F. Shallow Water Bathymetry Derived from Green Wavelength Terrestrial Laser Scanner. *Mar. Geod.* **2020**, *43*, 472–492. [\[CrossRef\]](#)
50. Letortu, P.; Costa, S.; Maquaire, O.; Delacourt, C.; Augereau, E.; Davidson, R.; Suanetz, S.; Nabucet, J. Retreat Rates, Modalities and Agents Responsible for Erosion along the Coastal Chalk Cliffs of Upper Normandy: The Contribution of Terrestrial Laser Scanning. *Geomorphology* **2015**, *245*, 3–14. [\[CrossRef\]](#)
51. Poursanidis, D.; Topouzelis, K.; Chrysoulakis, N. Mapping Coastal Marine Habitats and Delineating the Deep Limits of the Neptune's Seagrass Meadows Using Very High Resolution Earth Observation Data. *Int. J. Remote Sens.* **2018**, *39*, 8670–8687. [\[CrossRef\]](#)
52. Traganos, D.; Aggarwal, B.; Poursanidis, D.; Topouzelis, K.; Chrysoulakis, N.; Reinartz, P. Towards Global-Scale Seagrass Mapping and Monitoring Using Sentinel-2 on Google Earth Engine: The Case Study of the Aegean and Ionian Seas. *Remote Sens.* **2018**, *10*, 1227. [\[CrossRef\]](#)
53. Rende, S.F.; Bosman, A.; Di Mento, R.; Bruno, F.; Lagudi, A.; Irving, A.D.; Dattola, L.; Di Giambattista, L.; Lanera, P.; Proietti, R.; et al. Ultra-High-Resolution Mapping of *Posidonia oceanica* (L.) Delile Meadows through Acoustic, Optical Data and Object-Based Image Classification. *J. Mar. Sci. Eng.* **2020**, *8*, 647. [\[CrossRef\]](#)

54. Doukari, M.; Katsanevakis, S.; Soualakellis, N.; Topouzelis, K. The Effect of Environmental Conditions on the Quality of UAS Orthophoto-Maps in the Coastal Environment. *ISPRS Int. J. Geo-Inform.* **2021**, *10*, 18. [\[CrossRef\]](#)
55. Tzafaridi, V.M.; Petsimeris, I.; Hasiotis, T. Evaluation of Habitat Distribution and Human Imprints around an Insular Open-Pit, Gyalí Island, Southeast Aegean Sea. In Proceedings of the Tenth International Conference on Remote Sensing and Geoinformation of the Environment (RSCy2024), Paphos, Cyprus, 8–9 April 2024; Volume 13212, pp. 87–95. [\[CrossRef\]](#)
56. Borrelli, M.; Smith, T.L.; Mague, S.T. Vessel-Based, Shallow Water Mapping with a Phase-Measuring Sidescan Sonar. *Estuaries Coasts* **2022**, *45*, 961–979. [\[CrossRef\]](#)
57. Dimas, X.; Fakiris, E.; Christodoulou, D.; Georgiou, N.; Geraga, M.; Papathanasiou, V.; Orfanidis, S.; Kotomatas, S.; Papatheodorou, G. Marine Priority Habitat Mapping in a Mediterranean Conservation Area (Gyaros, South Aegean) through Multi-Platform Marine Remote Sensing Techniques. *Front. Mar. Sci.* **2022**, *9*, 953462. [\[CrossRef\]](#)
58. Kassouk, Z.; Ayari, E.; Deffontaines, B.; Ouaja, M. Monitoring Coastal Evolution and Geomorphological Processes Using Time-Series Remote Sensing and Geospatial Analysis: Application Between Cape Serrat and Kef Abbed, Northern Tunisia. *Remote Sens.* **2024**, *16*, 3895. [\[CrossRef\]](#)
59. Chatzipavlis, A.; Andreadis, O.; Psarros, F.; Hasiotis, T.; Velegrakis, A.; Evagorou, E.; Loizídi, M.; Chrysostomou, G. Morphological Changes Recorded from an Automated Beach Optical Monitoring System in a Highly Touristic Pocket Beach, Coral Bay, Pegeia, Cyprus. In Proceedings of the 18th International Conference on Environmental Science and Technology, Athens, Greece, 30 August–2 September 2023; pp. 1–4.
60. Jessin, J.; Heinzle, C.; Long, N.; Serre, D. A Systematic Review of UAVs for Island Coastal Environment and Risk Monitoring: Towards a Resilience Assessment. *Drones* **2023**, *7*, 206. [\[CrossRef\]](#)
61. Kovanič, L.; Topitzer, B.; Peřovský, P.; Blišťan, P.; Gergel'ová, M.B.; Blišťanová, M. Review of Photogrammetric and Lidar Applications of UAV. *Appl. Sci.* **2023**, *13*, 6732. [\[CrossRef\]](#)
62. *Labshere Reflectance Materials and Coatings—Technical Guide*; Labsphere, Inc.: North Sutton, NH, USA, 2011.
63. Rees, W.G. *Physical Principles of Remote Sensing*, 3rd ed.; Cambridge University Press: New York, NY, USA, 2013; ISBN 978-1-107-00473-3.
64. NASA Landsat Science: A Lambertian Reflector. Available online: <https://landsat.gsfc.nasa.gov/about/lambertian-reflector> (accessed on 13 April 2025).
65. Ponce-Alcántara, S.; Arangú, A.V.; Plaza, G.S. The Importance of Optical Characterization of PV Backsheets in Improving Solar Module Power. In Proceedings of the 8th International Photovoltaic Power Generation Conference Exhibition, Shanghai, China, 11–13 June 2015.
66. Padró, O.-C.; Muñoz, F.-J.; Ávila, L.Á.; Pesquer, L.; Pons, X. Radiometric Correction of Landsat-8 and Sentinel-2A Scenes Using Drone Imagery in Synergy with Field Spectroradiometry. *J. Remote Sens.* **2018**, *10*, 1687. [\[CrossRef\]](#)
67. Padró, J.; Carabassa, V.; Balagué, J.; Brotons, L.; Alcañiz, J.M.; Pons, X. Monitoring Opencast Mine Restorations Using Unmanned Aerial System (UAS) Imagery. *Sci. Total Environ.* **2019**, *657*, 1602–1614. [\[CrossRef\]](#)
68. Jeong, Y.; Yu, J.; Wang, L.; Shin, H.; Koh, S.M.; Park, G. Cost-Effective Reflectance Calibration Method for Small UAV Images. *Int. J. Remote Sens.* **2018**, *39*, 7225–7250. [\[CrossRef\]](#)
69. Jiang, S.; Jiang, C.; Jiang, W. Efficient Structure from Motion for Large-Scale UAV Images: A Review and a Comparison of SfM Tools. *ISPRS J. Photogramm. Remote Sens.* **2020**, *167*, 230–251. [\[CrossRef\]](#)
70. Alexiou, S.; Deligiannakis, G.; Pallikarakis, A.; Papanikolaou, I.; Psomiadis, E.; Reichert, K. Comparing High Accuracy T-LiDAR and UAV-SfM Derived Point Clouds for Geomorphological Change Detection. *ISPRS Int. J. Geo-Inform.* **2021**, *10*, 367. [\[CrossRef\]](#)
71. Storch, M.; Kisliuk, B.; Jarmer, T.; Waske, B.; de Lange, N. Comparative Analysis of UAV-Based LiDAR and Photogrammetric Systems for the Detection of Terrain Anomalies in a Historical Conflict Landscape. *Sci. Remote Sens.* **2025**, *11*, 100191. [\[CrossRef\]](#)
72. Agisoft LLC Agisoft Metashape 2024. Available online: <https://www.agisoft.com> (accessed on 13 April 2025).
73. Esri ArcGIS Pro 2024. Available online: <https://www.esri.com/en-us/arcgis/products/arcgis-pro/overview> (accessed on 13 April 2025).
74. Amodio, A.M.; Di Paola, G.; Roskopf, C.M. Monitoring Coastal Vulnerability by Using DEMs Based on UAV Spatial Data. *ISPRS Int. J. Geo-Inform.* **2022**, *11*, 155. [\[CrossRef\]](#)
75. Pagán, J.I.; Bañón, L.; López, I.; Bañón, C.; Aragonés, L. Monitoring the Dune-Beach System of Guardamar Del Segura (Spain) Using UAV, SfM and GIS Techniques. *Sci. Total Environ.* **2019**, *687*, 1034–1045. [\[CrossRef\]](#)
76. Chapapria, V.E.; Peris, J.S.; González-Escrivá, J.A. Coastal Monitoring Using Unmanned Aerial Vehicles (UAVs) for the Management of the Spanish Mediterranean Coast: The Case of Almenara-Sagunto. *Int. J. Environ. Res. Public Health* **2022**, *19*, 5457. [\[CrossRef\]](#) [\[PubMed\]](#)
77. Leica Geosystems AG Leica Cyclone 2024. Available online: <https://leica-geosystems.com/products/laser-scanners/software/leica-cyclone/leica-cyclone-register-360> (accessed on 13 April 2025).
78. CloudCompare CloudCompare (Version 2.12.4) [GPL Software] 2022. Available online: <https://www.cloudcompare.org> (accessed on 13 April 2025).

79. Lague, D.; Brodu, N.; Leroux, J. Accurate 3D Comparison of Complex Topography with Terrestrial Laser Scanner: Application to the Rangitikei Canyon (N-Z). *ISPRS J. Photogramm. Remote Sens.* **2013**, *82*, 10–26. [CrossRef]
80. Autodesk AutoCAD Civil 3D 2018. Available online: <https://www.autodesk.com/products/autocad-civil-3d/overview> (accessed on 13 April 2025).
81. Folk, R.L. *Petrologie of Sedimentary Rocks*; Hemphill's: Austin, TX, USA, 1980; ISBN 0-914696-14-9.
82. Blott, S.J.; Pye, K. GRADISTAT: A Grain Size Distribution and Statistics Package for the Analysis of Unconsolidated Sediments. *Earth Surf. Process. Landf.* **2001**, *26*, 1237–1248. [CrossRef]
83. McFeeters, S.K. The Use of the Normalized Difference Water Index (NDWI) in the Delineation of Open Water Features. *Int. J. Remote Sens.* **1996**, *17*, 1425–1432. [CrossRef]
84. Stumpf, R.P.; Holderied, K.; Sinclair, M. Determination of Water Depth with High-Resolution Satellite Imagery over Variable Bottom Types. *Limnol. Oceanogr.* **2003**, *48*, 547–556. [CrossRef]
85. Kayhan, E.C.; Ekmekcioğlu, Ö. Coupling Different Machine Learning and Meta-Heuristic Optimization Techniques to Generate the Snow Avalanche Susceptibility Map in the French Alps. *Water* **2024**, *16*, 3247. [CrossRef]
86. Sun, S.; Huang, R. An Adaptive K-Nearest Neighbor Algorithm. In Proceedings of the 2010 Seventh International Conference on Fuzzy Systems and Knowledge Discovery, Yantai, China, 10–12 August 2010; Volume 1, pp. 91–94. [CrossRef]
87. Fix, E.; Hodges, J.L. Discriminatory Analysis. Nonparametric Discrimination: Consistency Properties. *Int. Stat. Rev./Rev. Int. Stat.* **1989**, *57*, 238. [CrossRef]
88. Nababan, B.; Mastu, L.O.K.; Idris, N.H.; Panjaitan, J.P. Shallow-Water Benthic Habitat Mapping Using Drone with Object Based Image Analyses. *Remote Sens.* **2021**, *13*, 4452. [CrossRef]
89. Valderrama-Landeros, L.; Flores-de-Santiago, F.; Álvarez-Sánchez, L.F.; Flores-Verdugo, F.; Rodríguez-Sobreyra, R. The Influence of Spatial Resolution on Coastline Detection by Means of Multisource Remote Sensing Data. *Remote Sens. Appl. Soc. Environ.* **2024**, *35*, 101258. [CrossRef]
90. Chen, C.; Chen, H.; Liang, J.; Huang, W.; Xu, W.; Li, B.; Wang, J.; Wu, Q.; Shen, X.; Li, J.; et al. Extraction of Water Body Information from Remote Sensing Imagery While Considering Greenness and Wetness Based on Tasseled Cap Transformation. *Remote Sens.* **2022**, *14*, 3001. [CrossRef]
91. PLANET Planet Imagery Product Specifications. 2023. Available online: https://assets.planet.com/docs/Planet_Combined_Imagery_Product_Specs_letter_screen.pdf (accessed on 13 April 2025).
92. Melet, A.; Teatini, P.; Le Cozannet, G.; Jamet, C.; Conversi, A.; Benveniste, J.; Almar, R. Earth Observations for Monitoring Marine Coastal Hazards and Their Drivers. *Surv. Geophys.* **2020**, *41*, 1489–1534. [CrossRef]
93. United Nations Framework Convention on Climate Change; Executive Committee of the Warsaw International Mechanism for loss and Damage. *Policy Brief: Technologies for Averting, Minimizing and Addressing Loss and Damage in Coastal Zones*; United Nations Framework Convention on Climate Change; Executive Committee of the Warsaw International Mechanism for loss and Damage: Bonn, Germany, 2020. Available online: <https://unfccc.int/process-and-meetings/bodies/constituted-bodies/key-knowledge-products-2023/2024/executive-committee-of-the-warsaw-international-mechanism-for-loss-and-damage/policy-brief-technologies-for-averting-minimizing-and-addressing-loss-and-damage-in-coastal> (accessed on 13 April 2025).
94. Wicaksono, P.; Wulandari, S.A.; Lazuardi, W.; Munir, M. Sentinel-2 Images Deliver Possibilities for Accurate and Consistent Multi-Temporal Benthic Habitat Maps in Optically Shallow Water. *Remote Sens. Appl. Soc. Environ.* **2021**, *23*, 100572. [CrossRef]
95. Chatzipavlis, A.; Tsekouras, G.E.; Trygonis, V.; Velegrakis, A.F.; Tsimikas, J.; Rigos, A.; Hasiotis, T.; Salmas, C. Modeling Beach Realignment Using a Neuro-Fuzzy Network Optimized by a Novel Backtracking Search Algorithm. *Neural Comput. Appl.* **2018**, *31*, 1747–1763. [CrossRef]
96. Casella, E.; Drechsel, J.; Winter, C.; Benninghoff, M.; Rovere, A. Accuracy of Sand Beach Topography Surveying by Drones and Photogrammetry. *Geo-Mar. Lett.* **2020**, *40*, 255–268. [CrossRef]
97. Alessio, P.; Keller, E.A. Short-Term Patterns and Processes of Coastal Cliff Erosion in Santa Barbara, California. *Geomorphology* **2020**, *353*, 106994. [CrossRef]
98. Tyszkowski, S.; Zbucki, Ł.; Kaczmarek, H.; Duszyński, F.; Strzelecki, M.C. Terrestrial Laser Scanning for the Detection of Coastal Changes along Rauk Coasts of Gotland, Baltic Sea. *Remote Sens.* **2023**, *15*, 1667. [CrossRef]
99. Roulland, T.; Maquaire, O.; Costa, S.; Medjkane, M.; Davidson, R.; Fauchard, C.; Antoine, R. Seasonal Activity Quantification of Coast Badlands by TLS Monitoring over Five Years at the “Vaches Noires” Cliffs (Normandy, France). *Geomorphology* **2022**, *400*, 108083. [CrossRef]
100. Ashphaq, M.; Srivastava, P.K.; Mitra, D. Review of Near-Shore Satellite Derived Bathymetry: Classification and Account of Five Decades of Coastal Bathymetry Research. *J. Ocean Eng. Sci.* **2021**, *6*, 340–359. [CrossRef]
101. Casal, G.; Hedley, J.D.; Monteys, X.; Harris, P.; Cahalane, C.; McCarthy, T. Satellite-Derived Bathymetry in Optically Complex Waters Using a Model Inversion Approach and Sentinel-2 Data. *Estuar. Coast. Shelf Sci.* **2020**, *241*, 106814. [CrossRef]
102. Vrdoljak, L.; Kilić Pamuković, J. Assessment of Atmospheric Correction Processors and Spectral Bands for Satellite-Derived Bathymetry Using Sentinel-2 Data in the Middle Adriatic. *Hydrology* **2022**, *9*, 215. [CrossRef]

103. Evagorou, E.; Mettas, C.; Agapiou, A.; Themistocleous, K.; Hadjimitsis, D. Bathymetric Maps from Multi-Temporal Analysis of Sentinel-2 Data: The Case Study of Limassol, Cyprus. *Adv. Geosci.* **2019**, *45*, 397–407. [\[CrossRef\]](#)
104. Li, Z.; Peng, Z.; Zhang, Z.; Chu, Y.; Xu, C.; Yao, S.; García-Fernández, Á.F.; Zhu, X.; Yue, Y.; Levers, A.; et al. Exploring Modern Bathymetry: A Comprehensive Review of Data Acquisition Devices, Model Accuracy, and Interpolation Techniques for Enhanced Underwater Mapping. *Front. Mar. Sci.* **2023**, *10*, 1178845. [\[CrossRef\]](#)
105. Apostolopoulos, D.N.; Nikolakopoulos, K.G. Assessment and Quantification of the Accuracy of Low- and High-Resolution Remote Sensing Data for Shoreline Monitoring. *ISPRS Int. J. Geo-Inform.* **2020**, *9*, 391. [\[CrossRef\]](#)
106. Alevizos, E.; Roussos, A.; Alexakis, D.D. Geomorphometric Analysis of Nearshore Sedimentary Bedforms from High-Resolution Multi-Temporal Satellite-Derived Bathymetry. *Geocarto Int.* **2022**, *37*, 8906–8923. [\[CrossRef\]](#)
107. Wei, C.; Xiao, Y.; Fu, D.; Zhou, T. Impact of Turbidity on Satellite-Derived Bathymetry: Comparative Analysis Across Seven Ports in the South China Sea. *Remote Sens.* **2024**, *16*, 4349. [\[CrossRef\]](#)
108. Papakonstantinou, A.; Stamati, C.; Topouzellis, K. Comparison of True-Color and Multispectral Unmanned Aerial Systems Imagery for Marine Habitat Mapping Using Object-Based Image Analysis. *Remote Sens.* **2020**, *12*, 554. [\[CrossRef\]](#)
109. Ventura, D.; Bruno, M.; Jona Lasinio, G.; Belluscio, A.; Ardizzone, G. A Low-Cost Drone Based Application for Identifying and Mapping of Coastal Fish Nursery Grounds. *Estuar. Coast. Shelf Sci.* **2016**, *171*, 85–98. [\[CrossRef\]](#)

Disclaimer/Publisher’s Note: The statements, opinions and data contained in all publications are solely those of the individual author(s) and contributor(s) and not of MDPI and/or the editor(s). MDPI and/or the editor(s) disclaim responsibility for any injury to people or property resulting from any ideas, methods, instructions or products referred to in the content.